

The life cycles of Be viscous decretion discs: Time-dependent modelling of infrared continuum observations

R. G. Vieira^{1*}, A. C. Carciofi¹, J. E. Bjorkman², Th. Rivinius³, D. Baade⁴ and L. R. Rímulo¹

¹*Instituto de Astronomia, Geofísica e Ciências Atmosféricas, Universidade de São Paulo, Rua do Matão 1226, Cidade Universitária, 05508-900 São Paulo, SP, Brazil*

²*Ritter Observatory, Department of Physics & Astronomy, University of Toledo, Toledo, OH 43606, USA*

³*ESO - European Organisation for Astronomical Research in the Southern Hemisphere, Casilla 19001, Santiago 19, Chile*

⁴*ESO - European Organisation for Astronomical Research in the Southern Hemisphere, Karl-Schwarzschild-Str. 2, 85748 Garching bei München, Germany*

Accepted 2016 October 3. Received 2016 September 26; in original form 2016 May 16

ABSTRACT

We apply the viscous decretion disc (VDD) model to interpret the infrared disc continuum emission of 80 Be stars observed in different epochs. In this way, we determined 169 specific disc structures, namely their density scale, ρ_0 , and exponent, n . We found that the n values range mainly between 1.5 and 3.5, and ρ_0 varies between 10^{-12} and 10^{-10} g cm⁻³, with a peak close to the lower value. Our large sample also allowed us to firmly establish that the discs around early-type stars are denser than in late-type stars. Additionally, we estimated the disc mass decretion rates and found that they range between 10^{-12} and 10^{-9} M_⊙ yr⁻¹. These values are compatible with recent stellar evolution models of fast-rotating stars. One of the main findings of this work is a correlation between the ρ_0 and n values. In order to find out whether these relations can be traced back to the evolution of discs or have some other origin, we used the VDD model to calculate temporal sequences under different assumptions for the time profile of the disc mass injection. The results support the hypothesis that the observed distribution of disc properties is due to a common evolutionary path. In particular, our results suggest that the timescale for disc growth, during which the disc is being actively fed by mass injection episodes, is shorter than the timescale for disc dissipation, when the disc is no longer fed by the star and dissipates as a result of the viscous diffusion of the disc material.

Key words: circumstellar matter – radiative transfer – stars: emission-line, Be – stars: mass-loss.

1 INTRODUCTION

Be stars are early-type objects with ionized gaseous discs. The flattened geometry of these circumstellar structures was first suggested by [Struve \(1931\)](#), which was confirmed many years later by interferometric observations (e.g., [Dougherty & Taylor 1992](#); [Stee et al. 1995](#); [Quirrenbach et al. 1997](#)). Based on the observed fraction of Be-shell stars, [Porter \(1996\)](#) estimated a value of 5° for the disc opening angle, while [Quirrenbach et al. \(1997\)](#) found an upper limit of 20° from interferometric and spectropolarimetric observations. In particular, [Wood et al. \(1997\)](#) found a disc opening angle of 2.5° using spectropolarimetry. The

apparent inconsistency among these determinations can be explained by the disc flaring at larger radii, and the fact that distinct observational techniques probe different disc regions (e.g., [Carciofi 2011](#)). Based on the study of Fe II shell line profiles, [Hanuschik \(1996\)](#) showed that the observations are consistent with a rotationally supported geometrically thin disc in vertical hydrostatic equilibrium.

[Waters et al. \(1987\)](#) determined the disc density structure of 54 Be stars based on their *IRAS* infrared (IR) flux excesses. By assuming an outflowing disc model with a power law density profile, a fixed opening angle of 15°, and a radial velocity at the disc base of 5 km s⁻¹, they constrained the density slope exponent to be in the range between 2 and 3.5, and the mass loss rates, \dot{M} , to typically lie between 10^{-9} and 10^{-7} M_⊙ yr⁻¹. Based on the upper limit of

* E-mail: rg.vieira@gmail.com

their observed $\dot{M} - L_\star$ distribution, these authors also suggested a \dot{M} regime transition at $\sim 10^3 L_\odot$. These results still remain as a reference for typical Be disc properties (e.g., Granada et al. 2013). Such \dot{M} values are usually much larger than those found for normal B stars, which range from 10^{-11} to $3 \times 10^{-9} M_\odot \text{ yr}^{-1}$ (Snow 1981).

In the past decade, major steps forward were achieved in our understanding of Be star discs (see the recent review paper by Rivinius et al. 2013). The viscous decretion disc (VDD) model (Lee et al. 1991) became the new paradigm for the interpretation of Be stars observations (Carciofi 2011). For a handful of objects, detailed modeling using the VDD model has successfully reproduced multi-technique observations (e.g., Carciofi et al. 2006; Tycner et al. 2008; Jones et al. 2008; Carciofi et al. 2009; Klement et al. 2015). In addition to static models, the VDD model also allows the study of the dynamical evolution of the disc. For example, Carciofi et al. (2012) successfully described the light curve of 28 CMA using the time-dependent VDD model, providing the first determination of the viscosity parameter for a Be star disc. In particular, Haubois et al. (2012) showed how the observed light curves are affected by the mass injection rate history, and related the density exponent to the disc dynamical state. They found that steep radial density profiles typically correspond to the disc build-up phase, while flatter density slopes are usually related to the disc dissipation. Based on smoothed particle hydrodynamic (SPH) simulations, Okazaki et al. (2002) and Panoglou et al. (2016) demonstrated that flatter density profiles may also be related to the accumulation effect caused by binary interaction.

To relate the VDD dynamical predictions to observations, it is necessary to compute the radiative transfer in the circumstellar environment. State-of-the-art codes, such as HDUST (Carciofi & Bjorkman 2006, 2008) and BEDISK (Sigut & Jones 2007), are capable of solving the three-dimensional non-LTE radiative transfer problem, computing the disc continuum emission, polarization and line profiles for the VDD model. In particular, Vieira et al. (2015) developed the pseudo-photosphere model, which consists of a simple and accurate semi-analytic formulation to compute the disc continuum emission. It separates the disc into two components: an inner optically thick region (the pseudo-photosphere) and an outer optically thin region. Such simplification allows one to derive analytical expressions for the disc flux and spectral slope, which were calibrated and validated by the full radiative transfer calculations of HDUST. Based on this new approach, Vieira et al. (2015) showed that the spectral slope is mainly determined by the density radial slope and disc flaring exponent, and is rather insensitive to the base density and disc inclination. As a first application, Vieira et al. (2015) fitted the IRAS flux excess of a sub-sample of stars presented by Waters et al. (1987) to constrain the disc parameters. Among other results, they found that the mass decretion rate derived for this small sample lies between 10^{-12} and $10^{-9} M_\odot \text{ yr}^{-1}$, which is at least two orders of magnitude smaller than the values previously found by Waters et al. (1987). This difference arises from the application of the VDD model rather than Waters et al.'s outflowing disc model. For a viscosity parameter $\alpha = 1$, the VDD model predicts a radial velocity at the disc base of $v_\varpi \sim 10^{-3} c_s \sim 10^{-2} \text{ km s}^{-1}$, where c_s is the

sound speed in the disc (Krtićka et al. 2011). This value is much smaller than the outflow velocity of 5 km s^{-1} adopted by Waters et al. (1987).

Observational evidence has strengthened our confidence in the VDD model, and there have been many IR missions since IRAS and Waters et al. (1987) presented their results. In light of these theoretical and observational advancements, it is now time to revisit the Waters et al. study, using more recent observations and a better theoretical formalism. In this work, we extend the pseudo-photosphere model to include the stellar rotation effects, and a better prescription for the stellar flux attenuated by the disc. Using this model, we investigate the disc properties of 80 Be stars, based on their IR spectral energy distribution (SED). The model improvements are described in Section 2. Next, we list the sample selection criteria (Section 3), and present the SED fits (Section 4). Finally, we interpret our results using VDD hydrodynamical simulations (Section 5), and the conclusions follow.

2 THE PSEUDO-PHOTOSPHERE MODEL

The pseudo-photosphere is defined as the region where $\tau \geq \bar{\tau}$, where τ is the total disc optical depth along the line of sight, and $\bar{\tau}$ is a free parameter close to one. The model assumes a geometrically thin isothermal disc at temperature $T_d = f T_{\text{eff}}$, where $f = 0.6$ (Carciofi & Bjorkman 2006) and T_{eff} is the stellar effective temperature. The simplified parametric description of a VDD density profile is given by (e.g., Bjorkman & Carciofi 2005):

$$\rho(\varpi, z) = \rho_0 \left(\frac{\varpi}{R_{\text{eq}}} \right)^{-n} \exp \left(-\frac{z^2}{2H^2} \right), \quad (1)$$

where ρ_0 is the disc base density, R_{eq} is the equatorial stellar radius, ϖ and z are respectively the radial and vertical cylindrical coordinates in the stellar frame of reference, $H \propto \varpi^\beta$ is the disc scale height, and β the disc flaring exponent. Vieira et al. (2015) derived a semi-analytic expression for the pseudo-photosphere size \bar{R} as a function of the stellar and disc parameters,

$$\bar{R} \propto [\rho_0^2 \lambda^{2+u}]^{1/(2n-\beta)}, \quad (2)$$

where

$$u = \frac{d \ln(g_{\text{ff}} + g_{\text{bf}})}{d \ln \lambda}, \quad (3)$$

and g_{ff} and g_{bf} are the free-free and bound-free gaunt factors, respectively. The model calibration and validation were made based on HDUST results (Carciofi & Bjorkman 2006). HDUST is a three-dimensional Monte Carlo radiative transfer (RT) code, capable of simultaneously solving the non-LTE hydrogen level populations, ionization fraction and electron temperature from the radiative equilibrium condition at each disc position. By adopting $\bar{\tau} = 1.3$, Vieira et al. (2015) reproduced the HDUST IR fluxes to within 10%. Finally, note the pseudo-photosphere model assumptions are only valid for disc inclinations $\lesssim 75^\circ$. Above this limit, the geometrically thin disc approximation no longer holds.

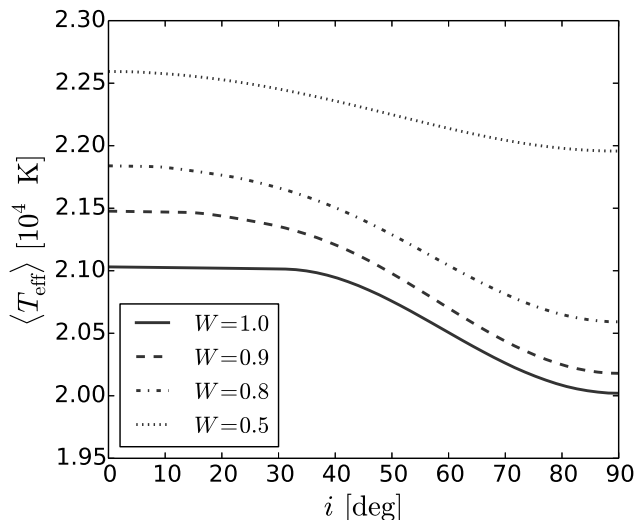


Figure 1. $\langle T_{\text{eff}} \rangle$ as a function of inclination. Each line represents a different stellar rotation rate, as indicated. The remaining stellar parameters (M_\star , R_{pole} and $\log L_\star$) correspond to a B2 sub-spectral type (Table 1).

2.1 Stellar rotation effects

Be stars are fast rotators (e.g., Porter 1996, Frémat et al. 2005, Rivinius et al. 2006). Although the stellar mass loss mechanism remains unknown, rotation close to the critical velocity ($W \equiv v_{\text{rot}}/v_{\text{orb}} \gtrsim 0.7$, Rivinius et al. 2013) certainly represents an important ingredient for the Be phenomenon. Aside from its relevance to the stellar evolution (Ekström et al. 2008, Georgy et al. 2013), the fast rotation also causes flattening and gravity darkening of the star (von Zeipel 1924). To take stellar oblateness into account in the pseudo-photosphere model, we employ the Roche approximation (e.g., Cranmer 1996; Ekström et al. 2008). The geometrical deformation of the star modifies the stellar emitting area, and also determines the fraction of the disc emission blocked by the star.

Rather than taking into account the detailed latitude dependence of the stellar surface effective temperature, we instead use its average value over the stellar hemisphere facing the observer:

$$\langle T_{\text{eff}} \rangle^4 = \frac{1}{A_\star} \int_{A_\star} T_{\text{eff}}^4(\theta) dA, \quad (4)$$

where A_\star is the stellar surface projected in the plane of the sky, θ is the stellar co-latitude,

$$T_{\text{eff}}(\theta) = \left(\frac{L_\star / \sigma_{\text{B}}}{\oint g^{4b} dA} \right)^{1/4} g^b(\theta), \quad (5)$$

(Cranmer 1996), L_\star the stellar luminosity, σ_{B} the Stefan-Boltzmann constant, and b is the gravity darkening exponent. The integral in the denominator is computed over the entire stellar surface, and we adopt the prescription described by Espinosa Lara & Rieutord (2011) to compute b for a given rotation rate. This average approximation is adequate for our purposes, since the total stellar flux is an integrated quantity. Figure 1 shows $\langle T_{\text{eff}} \rangle$ as a function of stellar rotation rate and inclination for a B2 star (see Table 1).

Table 1. List of adopted stellar parameters, derived from the interpolation of the evolutionary models computed by Georgy et al. (2013).

Parameter	Value			
Sp. Type	B1V	B2V	B3V	B7V
M_\star/M_\odot ^a	12.5	9.6	7.7	4.2
R_{pole}/R_\odot	6.7	5.6	4.9	3.7
$\log(L_\star/L_\odot)$	4.3	3.9	3.6	2.7
$\langle T_{\text{eff}} \rangle_{\text{pole}}/\text{K}$	24 800	21 800	19 300	13 150
$\langle T_{\text{eff}} \rangle_{\text{eq}}/\text{K}$	23 400	20 600	18 200	12 400
W ^b		0.8		
t/t_{MS}		0.75		

Note. ^aTownsend et al. (2004), ^b mean value for Be stars (Rivinius et al. 2013).

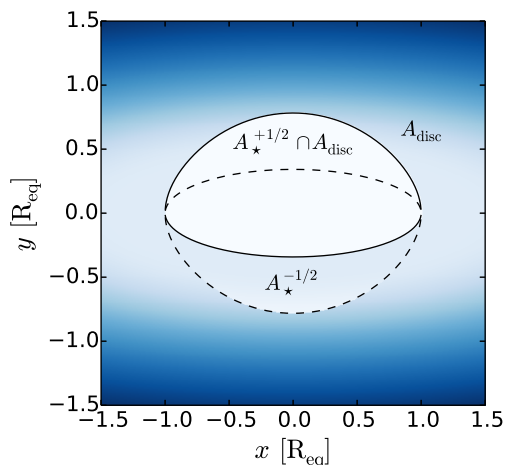


Figure 2. Synthetic image of a rotation-flattened star, surrounded by a gaseous disc. The solid line represents the contour of the stellar upper hemisphere ($A_\star^{+1/2}$), while the dashed contours represent the hidden stellar boundaries. The stellar lower hemisphere flux is attenuated by the disc opacity. The adopted parameters are $W = 0.8$, $i = 70^\circ$, $\bar{R}/R_{\text{eq}} = 2$ and $n = 3$. The disc size was assumed to be much larger than R_{eq} .

2.2 Stellar flux attenuation

The pseudo-photosphere model (Vieira et al. 2015) has three possible cases: (i) the general case, where both the pseudo-photosphere and tenuous region are present, (ii) the tenuous case, where the disc is entirely optically thin, and (iii) the case where the pseudo-photosphere is truncated, which means that \bar{R} exceeds the disc size. Different flux expressions were derived for each one of these cases. For simplicity, the detailed stellar extinction caused by the disc was neglected, and the stellar flux contribution either arises from both stellar hemispheres in the tenuous case, or only from the hemisphere above the stellar equator when the pseudo-photosphere is present. However, such approximation causes a spectral energy distribution (SED) slope discontinuity at λ' such that $\bar{R}(\lambda')/R_{\text{eq}} = 1$, which is more evident for higher inclinations. In order to remove this non-physical artifact, the pseudo-photosphere model flux expressions were generalized to properly include the stellar flux attenuation caused

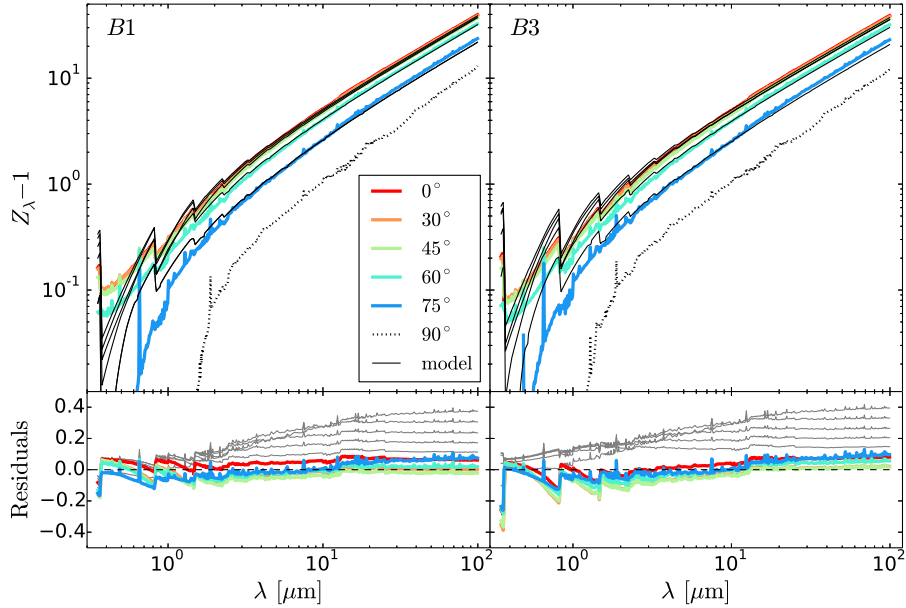


Figure 3. Comparison between the pseudo-photosphere model (thin black lines) and HDUST results (thick coloured lines), for a disc with $\rho_0 = 8.4 \times 10^{-12} \text{ g cm}^{-3}$ and $n = 3.5$. Upper panels: flux excesses computed with the pseudo-photosphere model (stellar rotation and attenuation effects included) superimposed on the HDUST results. Bottom panels: residual plots, comparing the HDUST results to the pseudo-photosphere model including (i) the stellar rotation effects (thick lines; colors representing disc inclination), and (ii) neglecting those effects (thin grey lines; the largest value corresponding to model with $i = 75^\circ$). The edge-on HDUST model (dotted line) is presented in the upper panels just for reference, since it does not have a pseudo-photosphere model counterpart. The adopted stellar parameters correspond to a B1 (left) and a B3-type (right), and are presented in Table 1.

by the disc. Consider the flux excess definition:

$$Z_\lambda = \frac{F_\lambda}{F_\lambda^\star}, \quad (6)$$

where F_λ is the total flux (star and disc combined),

$$F_\lambda^\star = \frac{A_\star}{d^2} S_\lambda^\star (\langle T_{\text{eff}} \rangle) \quad (7)$$

is the flux of the disc-less star, and S_λ^\star is the stellar surface brightness. To compute the stellar flux, we adopted interpolated models from [Castelli & Kurucz \(2003\)](#). The stellar brightness is assumed to be uniform (no limb darkening), and is a function of $\langle T_{\text{eff}} \rangle$. The new flux excess expression for the general case may be written as

$$Z_\lambda = \frac{\cos i \mathcal{F}}{A_\star / (\pi R_{\text{eq}}^2)} \left[\left(\bar{R} / R_{\text{eq}} \right)^2 \Psi - 1 \right] + Z_\lambda^{\text{num}}, \quad (8)$$

where

$$Z_\lambda^{\text{num}} = \frac{A_\star - A_\star^{-1/2}}{A_\star} + \frac{1}{A_\star} \int_{A_\star^{-1/2}} e^{-\tau} dA - \frac{1}{A_\star} \int_{A_\star^{+1/2} \cap A_{\text{disc}}} \mathcal{F} (1 - e^{-\tau}) dA \quad (9)$$

is the numerically computed flux excess component (see Figure 2 for the definitions of the integration domains),

$$\Psi = 1 + \frac{2\bar{\tau}}{2n - \beta - 2} \left[1 - (R_d / \bar{R})^{-2n + \beta + 2} \right], \quad (10)$$

$\mathcal{F} \equiv S_\lambda^\star / B_\lambda(T_d)$, R_d is the disc size, and τ follows the definition given by [Vieira et al. \(2015\)](#). Because of the complicated Roche model geometry, the integrals can only be

numerically evaluated (except for the trivial pole-on case). The derived expression now accounts for the attenuated stellar flux, and properly subtracts the disc flux contribution shadowed by the star. The expressions for the entirely tenuous disc and truncated pseudo-photosphere become, respectively,

$$Z_\lambda^{\text{tenuous}} = \frac{2\bar{\tau} \cos i \mathcal{F}}{A_\star / (\pi R_{\text{eq}}^2)} \left[\frac{1 - (R_d / R_{\text{eq}})^{-2n + \beta + 2}}{2n - \beta - 2} \right] \left(\bar{R} / R_{\text{eq}} \right)^{2n - \beta} + Z_\lambda^{\text{num}} \quad (11)$$

and

$$Z_\lambda^{\text{trunc}} = \frac{\cos i \mathcal{F}}{A_\star / (\pi R_{\text{eq}}^2)} \left[(R_d / R_{\text{eq}})^2 - 1 \right] + Z_\lambda^{\text{num}}. \quad (12)$$

The comparison between the newly derived formulae and HDUST results is presented in Figure 3. Like the previous version, the derived IR fluxes are accurate within 10% when compared to HDUST results. In the same figure, the bottom panels also show the residuals for the pseudo-photosphere model without the rotation effects. For this case, the residuals increase with inclination. At larger inclinations, the disc area hidden by the non-rotating star is larger than the one hidden by a flattened rotating star. Consequently, an important contribution of the disc flux is missed when rotation is neglected. The dependence of the magnitude excess as a function of the disc base density is presented in Figure 4.

3 SAMPLE SELECTION

[Frémat et al. \(2005\)](#) determined the fundamental parameters of 130 early-type stars based on their observed spectra,

taking into account the stellar rotation effects. To select our sample of Be stars from their list, the following criteria were applied:

- classical Be star classification;
- non-shell line profile designation;
- having at least two IR flux bands measured by the same mission (i.e., at similar epochs);
- observed IR spectral slope $d \ln F_\lambda / d \ln \lambda$ lying between -4 and -1.5 ;
- observed flux larger than the model stellar flux.

The IR flux data from the *IRAS* (Neugebauer et al. 1984), *AKARI/IRC* (Ishihara et al. 2010), and *AllWISE* (Wright et al. 2010) missions were used. Of the *AllWISE* fluxes, only those for 12 and 22 μm were used because the pseudo-photosphere model predictions are less reliable at $\lambda \lesssim 5 \mu\text{m}$ (Vieira et al. 2015). Excluding the *AllWISE* shorter wavelength measurements has the additional advantage that the three adopted IR missions then probe similar regions of the disc (*IRAS* provides fluxes at 12, 25 and 60 μm [we excluded 100 μm], and *AKARI/IRC* at 9 and 18 μm). Finally, upper limit measurements were also excluded from our analysis.

Special care was given to eliminate shell stars from the list of Frémat et al. (2005), because the model is valid only for $i \lesssim 75^\circ$. This was done by visually inspecting the spectra available in online repositories, such as *BeSS*¹, to exclude the objects with clear shell signatures. The objects whose inclination angle (as determined by Frémat et al.) that were larger than 75° without clear shell features in the spectrum were kept in our list. For these, the inclination angle was set to $i = 75^\circ \pm 10^\circ$. Criterion (e) ensures a disc is present at the time of the observations, and rules out flat/increasing slopes, which may be indicative of the presence of dust. Criterion (f) eliminates objects with inconsistent stellar parameters. After applying the above criteria, 80 out of the original 130 stars were selected. Their fluxes were color-corrected by computing the spectral slope from the catalogue values as a first guess (separately for each mission), and then using the mission bandpasses to iterate the monochromatic fluxes until convergence is achieved. The resulting fluxes are presented in Appendix A.

4 SED FITTING

The observed SEDs were fitted using the *emcee* code (Foreman-Mackey et al. 2013), a Markov chain Monte Carlo (MCMC) implementation. *emcee* samples the posterior probability in an n -dimensional parameter space, given a likelihood function ($\propto \exp[-\chi^2/2]$ in our case). For each simulation, we used 100 walkers (random-walk samplers) with 100 steps in the initial phase (burn-in) and 1000 steps in the final sampling phase (starting from the last state of the burn-in chain). The following parameters of the pseudo-photosphere model were kept fixed: $f = 0.6$, $\bar{\tau} = 1.3$, $\beta = 1.5$ and $R_d = 1000 R_{\text{eq}}$. The stellar parameters from Frémat et al. (2005; $T_{\text{eff},0}$, $\log g_0$, $v \sin i$ and V_c)², and the Hipparcos paral-

¹ <http://basebe.obspm.fr/basebe/>

² The “0” subscripts refer to the parent non-rotating counterpart parameters (pnrc), defined by Frémat et al. (2005).

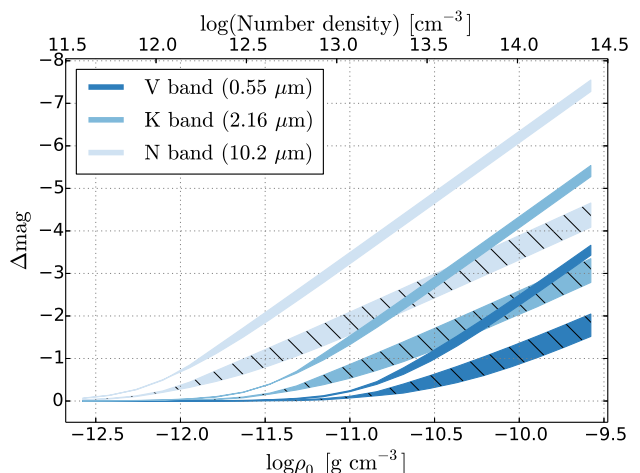


Figure 4. Disc flux excess (magnitudes) as a function of the disc base density for a *B2* star. The curve width covers disc inclinations from 0° to 75° (the pole-on case corresponds to the Δmag upper limit). The wavelength is specified by the blue shade, as indicated. The hatched curves correspond to an $n = 3.5$ model, while the non-hatched curves represent the $n = 2.5$ models.

Table 2. Disc inclinations derived from interferometric measurements. For the case of axial ratio measurements, we adopted the geometrically thin disc approximation $i = \cos^{-1}(\text{axial ratio})$.

HD	inclination	Reference
5394	$39.6^\circ \pm 1.8^\circ$	Quirrenbach et al. (1997)
23630	$41.1^\circ \pm 7.0^\circ$	Tycner et al. (2005)
25940	$40.4^\circ \pm 19.7^\circ$	Delaa et al. (2011)
37795	$35^\circ \pm 5^\circ$	Meilland et al. (2012)
50013	$35^\circ \pm 10^\circ$	Meilland et al. (2012)
58715	$46.4^\circ \pm 16.4^\circ$	Tycner et al. (2005)
89080	$65^\circ \pm 10^\circ$	Meilland et al. (2012)
91465	$70^\circ \pm 10^\circ$	Meilland et al. (2012)
105435	$35^\circ \pm 15^\circ$	Meilland et al. (2012)
120324	$25^\circ \pm 5^\circ$	Meilland et al. (2012)
158427	$45^\circ \pm 5^\circ$	Meilland et al. (2012)
217891	$45.4^\circ \pm 12.1^\circ$	Touhami et al. (2013)

axes were chosen to vary within their $1-\sigma$ confidence interval in the MCMC run. This procedure ensures that the uncertainties in the stellar parameters are properly accounted for when estimating the confidence intervals of the disc parameters. Appendix B describes how the stellar parameters of interest were estimated based on the parameters derived by Frémat et al. (2005).

When available, interferometric measurements were used to estimate the disc inclination (Table 2). Otherwise, a 10° confidence interval was adopted for the inclination values from Frémat et al. (2005), since their original confidence ranges were probably underestimated (Rivinius et al. 2013, see also the typical values of Table 2). Finally, no prior constraints were applied to the parameters of interest, n and $\log \rho_0$, except for restricting n to positive values. A total of 169 models were fitted with *emcee*, since many of the 80 objects were observed by different missions.

4.1 Results

The SED fitting results are presented in Appendix C (Table E2), where the median values of the derived posterior probability distributions are given. The derived uncertainties correspond to the 16th and 84th percentiles of these distributions, which are equivalent to a 1- σ Gaussian variance. The associated \bar{R} values, as well as a discussion about the effects of possible disc truncation effects caused by a binary companion are discussed in Appendix D. Table E2 also lists the values for the steady-state accretion rate, defined as

$$\dot{M}_{\text{SS}} = \frac{3\pi\sqrt{2\pi}\alpha R_{\text{eq}}^2 c_s^3 \rho_0}{V_{\text{crit}}^2 \left[(R_0/R_{\text{eq}})^{1/2} - 1 \right]}, \quad (13)$$

where α is the viscosity parameter (Shakura & Sunyaev 1973), $c_s = (kT_d/\mu m_H)^{1/2}$ is the isothermal sound velocity, $V_{\text{crit}} = \sqrt{GM_\star/R_{\text{eq}}}$ is the break-up velocity, M_\star is the stellar mass, T_d is the disc temperature, μ is the mean molecular weight of the gas, m_H is the atomic mass unity and k is the Boltzmann constant. The integration constant R_0 is approximated by the isothermal critical radius (Krtićka et al. 2011; Okazaki 2001):

$$\frac{R_0}{R_{\text{eq}}} = \frac{R_c}{R_{\text{eq}}} = \frac{3}{10} \left(\frac{V_{\text{crit}}}{c_s} \right)^2. \quad (14)$$

We emphasize however that Equation (13) is strictly true only for a disc fed long enough to approach a steady-state. The results from Eq. (13) should be regarded as estimates of the mass accretion rate, not true determinations.

Figure 5 shows the `emcee` sampling results for β CMi and 28 Cyg, as representative cases. In particular, the results found for β CMi are in very good agreement with those found by Klement et al. (2015), who found that the observations probing a more extended region of the disc are compatible with $n = 3$ and $\rho_0 = 2 \times 10^{-12} \text{ g cm}^{-3}$. Note there is a correlation between n and $\log \rho_0$, since different combinations of these parameters can result in a similar \bar{R} (see Equation 2). Conversely, the derived uncertainties for these parameters are also correlated (Table E2). Additionally, the results show that large n values ($n \gtrsim 3.5$, case of 28 Cyg) usually have broader confidence ranges (and, consequently, larger $\log \rho_0$ uncertainties). To understand this behaviour, one must recall that the spectral slope is mainly determined by n (Vieira et al. 2015), and has a weak dependence on $\log \rho_0$ and disc inclination. Figure 6 shows this dependence on n for two base densities. For a fixed uncertainty in the SED slope, the uncertainties for a large n are much larger than those for a smaller n value.

5 DISCUSSION

Figure 7 shows the disc parameters of the selected sample. The grey shading in the diagram was obtained by combining the posterior probabilities of n and ρ_0 for all 169 fitted SEDs, and normalizing its integral over the plane to unity. The median values of n and $\log \rho_0$ of individual stars are shown as the colored circles, color-coded to indicate the effective temperature of the star.

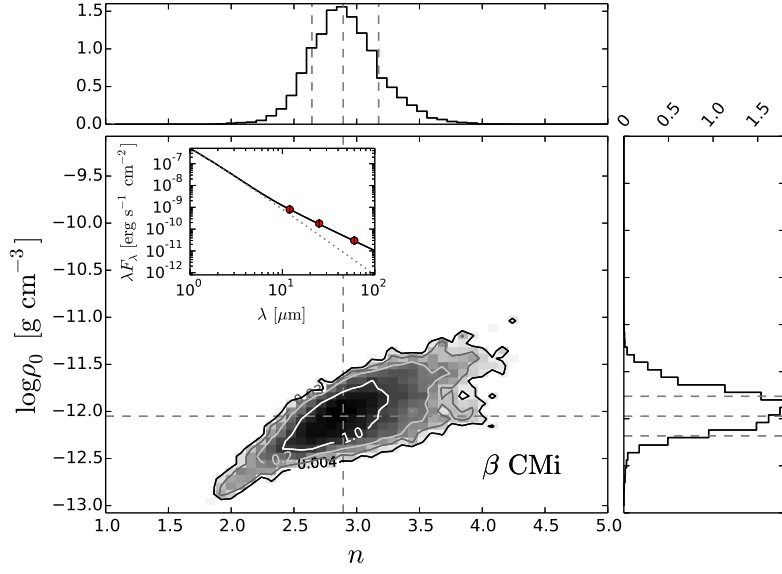
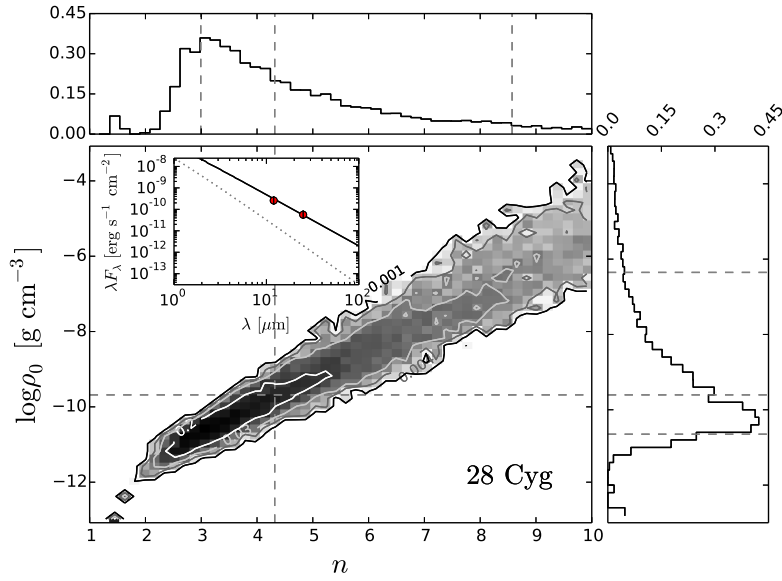
Note the correlation between n and $\log \rho_0$ along the high probability ridge of the shading plot. This cannot be due to

the correlation shown in the individual fits, since the uncertainties for $n < 5$ solutions lie typically between 0.1 and 0.5 for both parameters. The scatter distribution of n vs. $\log \rho_0$ has a Pearson's correlation coefficient of 0.57. There is a clear peak at $\log \rho_0 \simeq -12$, with the base density spreading over two orders of magnitude, while the n values preferentially occur between 1.5 and 3.5. Note the upper-left corner is practically empty.

Another important property of Figure 7 is that earlier-type stars are more likely to have denser discs, while cooler stars usually occupy the lower region of the diagram. This result can better be seen in Figure 8(a), where stars for all temperatures can reach about the same low values, but only hot stars can reach higher ones. On the other hand, Figure 8(b) shows no clear correlation between n and T_{eff} .

Figure 9 superimposes the previous results obtained by other authors on our distribution in the $n - \log \rho_0$ diagram. The choice of a disc flaring exponent of $\beta = 1$ made by Waters et al. (1987) is expected to result in values of n smaller than ours by a difference of 0.25. This occurs because the actual free parameter in both model formulations is $2n - \beta$ rather than n alone, as discussed by Vieira et al. (2015). If we consider the sub-sample of *IRAS* observations studied by Waters et al. (1987), the difference between our values of n and the ones from those authors indeed occurs more often around 0.25, although the differences range between -0.4 and 2.4. Possible reasons for these differences are: (i) our error estimates for n are typically about 0.2, i.e., of the same order that the expected differences; and (ii) the inclusion of rotation effects, not taken into account by Waters et al. (1987), affects the SED shape (see Fig. 3), and consequently the derived disc parameters. Despite of these effects, the general trend of the results found by Waters et al. (1987) shows a good agreement with our results. They occupy the higher probability ridge found in this work, and present the same trend with T_{eff} . However, the values obtained by Silaj et al. (2010) from the fit of $H\alpha$ profiles appear to be systematically denser than our models. Such a difference may be related to a selection bias in their sample, which consists of Be stars with strong $H\alpha$ emission, and hence denser discs. Furthermore, Silaj et al. states that only preliminary estimates could be given based on their not extensive adopted grid.

Figure 10 shows the relation between the stellar luminosity and the mass accretion rate. The estimated \dot{M}_{SS} values tend to be higher for more luminous objects. This may indicate that more massive stars can provide higher mass injection rates. But another possibility is that discs of more massive stars have smaller α values, thereby making the radial diffusion time scale and outflow velocities smaller. As found before by Vieira et al. (2015) for a smaller sample, our results for the mass accretion rates are up to three orders of magnitude smaller than the mass loss rates computed by Waters et al. (1987), and also show a larger scatter than that found by these authors. Additionally, we do not find the regime transition (i.e., a slope change in the dotted line) at $\log(L_\star/L_\odot) = 3$ suggested by Waters et al.. Consequently, our results do not suggest different ejection mechanisms for early- and late-type Be stars, as proposed by them. Interestingly, our \dot{M}_{SS} estimates are compatible with the \dot{M}_{disc} values calculated by Granada et al. (2013), which were based on a completely different approach. These authors proposed that the mechanical mass loss during the main-sequence evo-


 (a) Sampling of β CMi disc parameters.


(b) Sampling of 28 Cyg disc parameters.

Figure 5. Examples of the posterior probability distributions of disc parameters computed with the `emcee` code. The contour values indicate the probability density levels, with its integral normalized to unity. The SED fit is shown inset within the main panel, where the circles correspond to *IRAS* observations, the solid line represents the total flux, and the dotted line represents the photospheric flux. The dashed lines in the main panel indicate the 50th percentiles of the distributions (i.e., its median value). The upper and right panels show the probability densities for the individual parameters $\log \rho_0$ and n , respectively. The dashed lines correspond to the 16th, 50th, and 84th percentiles of their respective distributions (see text). Notice that panels (a) and (b) have different plot ranges.

lution is that necessary to remove the angular momentum excess from an over-critically rotating stellar surface. From that, they estimated the disc structure and mass decretion rates using the model from Krtićka et al. (2011).

5.1 Disc variability

Since the observations of each IR mission were taken in different epochs³, disc variability can also be studied. The variation of the disc parameters, based on *AKARI* and *AllWISE*

³ Mission epochs: *IRAS*: from January to November 1983; *AKARI/IRC*: from May 2006 to August 2007; and *AllWISE*: from January to November 2010.

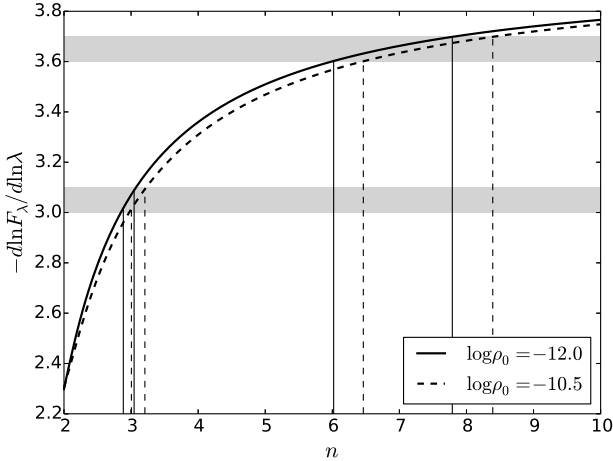


Figure 6. Spectral slope between $10\mu\text{m}$ and $20\mu\text{m}$ as a function of n , for two disc base densities. The horizontal grey bars indicate a confidence range of 0.1 (a typical value found for the observed SED slopes) at two arbitrary slope values. The vertical lines indicate the corresponding n confidence ranges. For both curves, we adopted a $B2$ spectral type (Table 1) and a pole-on orientation.

measurements, is presented in Figure 11. The two more recent missions were selected because they have a smaller time separation (~ 4 yr) and more accurate fluxes. Interestingly, there are many more arrows moving from the upper right corner to the lower left one (i.e., from high $\log \rho_0$ and n) than the reverse. Out of the 53 models plotted, 46 points downwards and only 7 upwards. The VDD model provides the key to understand this result.

5.1.1 Hydrodynamical interpretation

Following Haubois et al. (2012), we computed the time evolution of VDD density profiles with the SINGLEBE code (Okazaki 2007; Okazaki et al. 2002), and fed these to the LTE flux expression derived in Appendix E to compute the continuum fluxes at 12 , 25 and $60\mu\text{m}$ as a function of time. Then, the same procedure of Section 4 was used to obtain from each synthetic SED a pair of $\log \rho_0$ and n values from the pseudo-photosphere model.

Haubois et al. (2012) explored the time-dependent VDD model predictions for three cases of interest: (i) a forming disc with a constant mass injection rate, (ii) a dissipating disc with no mass injection, and (iii) a disc subject to a periodic mass injection. For a forming disc with a constant mass injection rate, the density radial profile is initially very steep, but progressively approaches the steady-state value ($n = 3.5$) during the disc build-up. Technically, a decretion disc never actually reaches the steady-state, since it takes an infinite time to do so (Okazaki 2007). However, as the disc build-up occurs from inside-out, the disc inner region approaches steady-state before the outer parts. Therefore, the disc observables that probe this inner region will appear similar to a steady-state disc (see Appendix E). For the case when fully developed discs have the mass injection rate suddenly turned-off, the material of the disc inner part is re-accreted due to the outward angular momentum transfer via the disc turbulent viscosity. The simultaneous infall in the inner disc and outflow in the outer disc gives rise to

a stagnation radius in the disc, where the radial velocity is zero. This stagnation radius slowly propagates outward, and the density structure within this radius evolves by decreasing its density level while maintaining its radial profile (Haubois et al. 2012, see also Appendix E).

Figure 12 shows the computed evolutionary tracks across the $n - \log \rho_0$ diagram (see Appendix E). In Figure 12(a), during the disc build-up, the disc parameters reach the steady-state strip ($n \sim 3.5$) in less than one year. Subsequently, the solution remains close to $n = 3.5$ as long as mass is provided to the disc. When the mass injection is turned-off, the inner disc quickly dissipates and the evolutionary tracks move toward the left-bottom position of the diagram. This direction coincides with the results seen in Figure 11, suggesting that most of the observed discs are in a dissipating state. Furthermore, disc dissipation takes a longer time than that required for its build-up (when fed by a constant mass injection rate), which makes dissipating discs more likely to be observed than forming ones. This explains why more arrows in Figure 11 point toward the lower left. Both build-up and dissipation time scales are expected to be comparable only in the case of small discs, since the dissipation time scale increases with disc size (e.g., Oktariani et al. 2016).

Another situation of interest is shown in Figure 12(b), where the disc is subjected to a periodic mass injection rate. The disc recovery is very fast, so the disc parameters rapidly reach the upper right portion of the loop. Again, the track asymptotically approaches the $n = 3.5$ steady-state value while material is fed to the disc. The subsequent part of the disc dissipation then produces the slower excursion along the lower left part of the diagram. A loop-like behaviour can be also found for many other pairs of measurements probing the disc, such as photometry in different bands (Haubois et al. 2012), polarimetry and Balmer discontinuity (Haubois et al. 2014), and even interferometry (Faes et al. in preparation).

Finally, it is useful to recall that the association of $n = 3.5$ to the disc steady-state is based on some model simplifications, such as disc isothermality and constant α (as a function of both position and time), and also assumes an isolated system (e.g., Bjorkman & Carciofi 2005). The change in the steady-state density exponent could be due to: (i) either an α and/or a T_d radial dependence (e.g., Carciofi & Bjorkman 2008, Equation 24); and (ii) the accumulation effect caused by a binary companion (Panoglou et al. 2016; Klement et al. 2015; Okazaki et al. 2002), which can reduce n to ~ 3 . For example, Klement et al. (2015) found evidence for disc truncation in β CMi with $n = 3$. For these reasons, we expect steady-state discs to have n in the range $3 \lesssim n \lesssim 3.5$.

5.2 The viscous disc life-cycle

From the representative examples shown in Figure 12, the time-dependent behaviour of the disc can be summarized in terms of regions in the $n - \log \rho_0$ diagram. Figure 13 shows the definition of such regions, divided into: forming discs ($n \gtrsim 3.5$); steady-state discs ($3 \lesssim n \lesssim 3.5$) and dissipating discs ($n \lesssim 3$). Since no stars are observed in the upper left region of the diagram, it is called the “forbidden zone”. Reaching this region would require either a (not observed) much higher $\dot{M}_{\text{SS}} (\gtrsim 10^{-8} M_{\odot} \text{yr}^{-1})$, or the presence of a closer/more massive binary companion. Finally, the de-

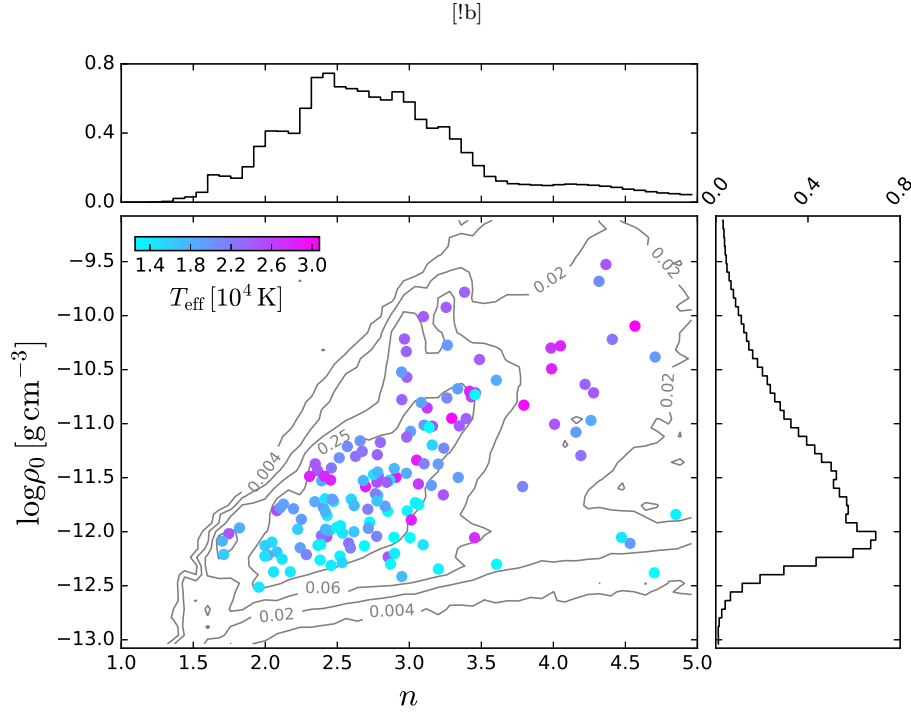
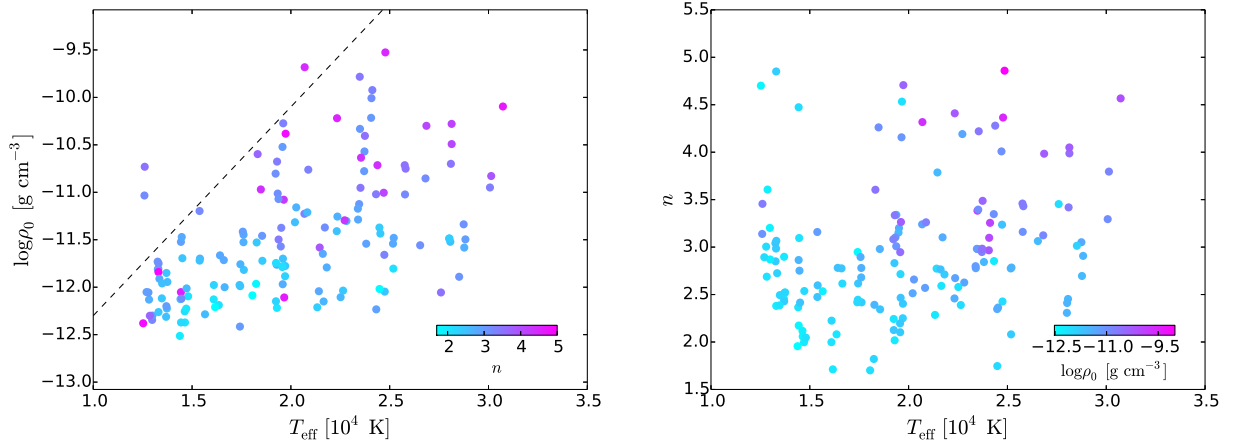


Figure 7. Disc density and slope of the sample of Be stars. Shown are the `emcee` results for the n and $\log \rho_0$ distributions. The main panel shows the probability density (grey scale contours), while the upper and left panels show the distribution for the individual parameters. These distributions correspond to the combination of all posterior probabilities derived with the `emcee` code, and their integral values were normalized to unity. The contour values correspond to the probability density levels. Superimposed, we plotted the median values of the `emcee` sampled distributions for the individual stars. The colors indicate the stellar effective temperature, computed by Frémat et al. (2005).



(a) ρ_0 as vs. T_{eff} . The colors indicate the respective n value, and (b) n vs. T_{eff} . The colors indicate the respective $\log \rho_0$ values. the dashed line indicate the upper limit of the scatter distribution.

Figure 8. Fitted parameters as a function of the stellar effective temperature. The models with $n > 5$ were excluded.

tection limit was defined as the line below which the flux excess emerging from the disc becomes negligible, as shown in Figure 4. This may be not the case for other disc observables (e.g., emission lines), which eventually can probe smaller densities.

From a total of 169 fitted models, 93 (55%) populate

the dissipating region, 40 (24%) are in the formation region. In this last group, 17 (10% of the total sample) have $n > 5$, which may also indicate a disc-less state. These numbers suggest that, on average for our sample, the disc dissipation takes ~ 2 times longer than the disc build-up. Rivinius et al. (1998) found a similar behaviour for the line emission vari-

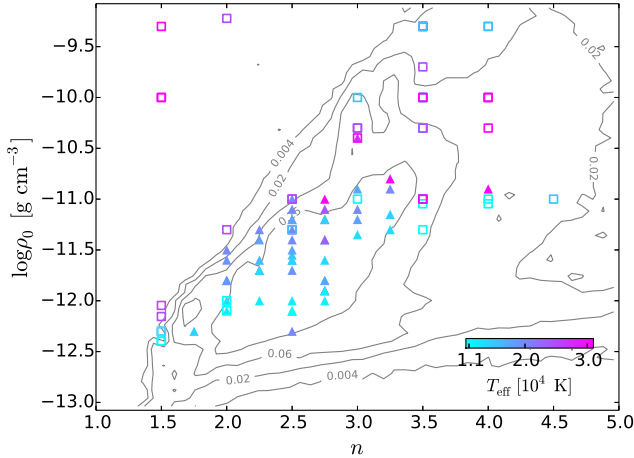


Figure 9. Previous results for n and $\log \rho_0$ found by Waters et al. (1987, solid triangles) and Silaj et al. (2010, open squares), superimposed on the contours of the probability density distribution found by the present work. The symbol colors correspond to the stellar effective temperature adopted by each work.

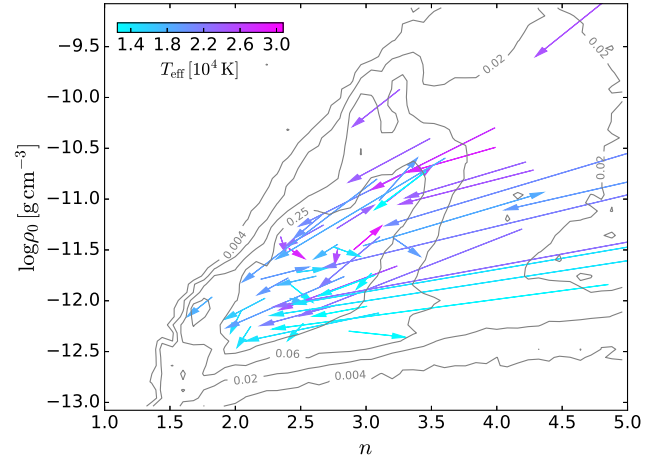


Figure 11. Evolution of the disc parameters between different epochs. The arrow tails correspond to values derived from *AKARI* observations, while the arrow heads correspond to determinations from *AllWISE* data. The arrows were superimposed on the probability distribution of the fitted parameters (see Figure 7), and their colors correspond to the effective temperature determined by Frémat et al. (2005).

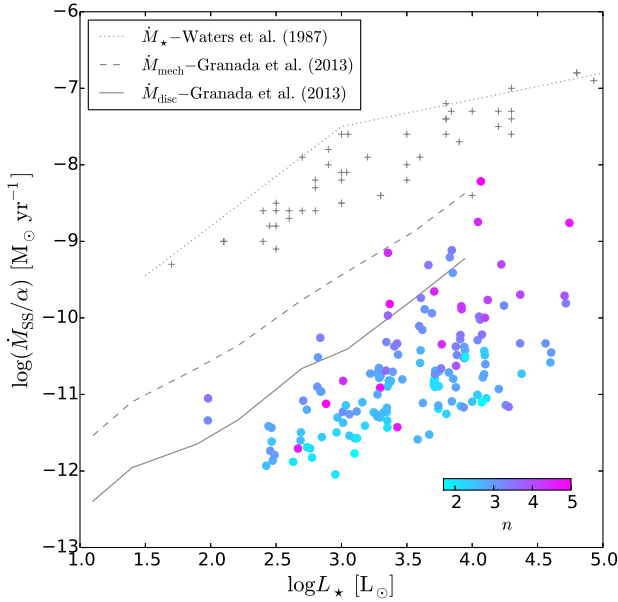
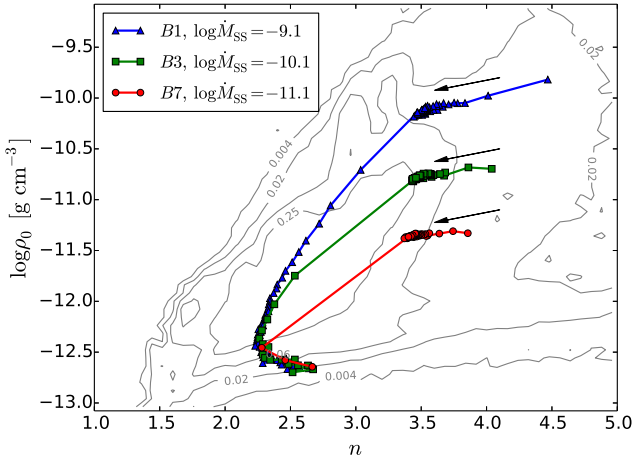


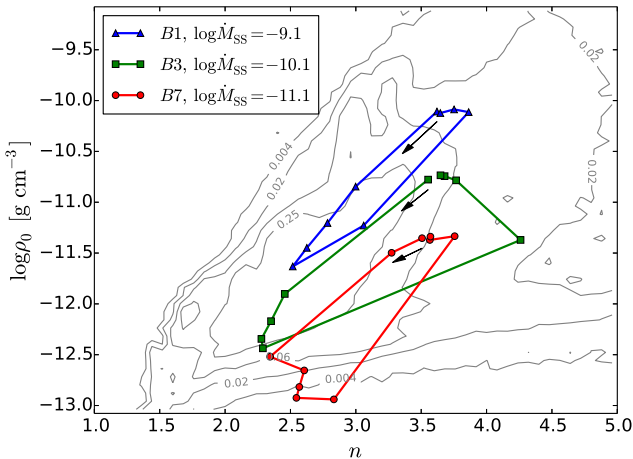
Figure 10. Mass accretion rate as a function of stellar luminosity. The circles represent the values estimated from the *emcee* results, while the crosses indicate the values computed by Waters et al. (1987). The circle colors indicate the fitted n value, and the $n > 5$ cases were excluded. The dotted line corresponds to the upper limit suggested by Waters et al. (1987). The dashed and solid lines correspond, respectively, to the mechanical loss rate and the mass accretion rate computed by Granada et al. (2013).

ability of μ Cen, where the observed outbursts are followed by extended relaxation phases. Similar results were found by Haubois et al. (2012) and Huat et al. (2009). In both cases, the dissipation time scales appear to be longer than the outburst episodes. Finally, only 36 models (21%) are found in the steady-state strip. According to the theoretical evolutionary tracks in Figure 12, the discs must be fed for long

enough to remain in the steady-state region. The smaller number of discs observed in the steady dynamical state suggests that the mass injection episodes are probably shorter than the duration of the dissipation phase, and therefore less likely to be observed.



(a) Disc build-up and dissipation. In this case, the disc is fed for 30 yr at a constant rate (portion from the right to $n \approx 3.4$ of the tracks), which is then turned-off for 60 yr. The arrows indicate the evolution direction, and the time step was held fixed at 6 months. In the plot, the steps where $Z_{12\mu\text{m}} - 1 < 0.05$ were omitted.



(b) Disc subjected to a periodic mass injection. The adopted period was 5 yr, with a constant mass injection rate for half of each cycle and none the other half. The time step was held fixed at 6 months, and the 11th cycle is shown (i.e., the initial time corresponds to 50 yr). The arrows indicate both track initial positions and direction of evolution.

Figure 12. Disc evolution across the $n - \log \rho_0$ diagram. The evolutionary tracks are superimposed on the probability distribution of the fitted parameters (see Figure 7). The disc models have viscosity parameter $\alpha = 1$ and pole-on orientation. The adopted mass decretion rates and spectral types are indicated.

6 CONCLUSIONS

We have systematically applied the VDD model to measure the disc properties of a large sample of Be stars using their IR SEDs. The MCMC method provided a reliable determination of the disc parameters of this sample at different epochs, producing a total of 169 models. The combination of the posterior probability distributions computed with `emcee` MCMC implementation showed that the density exponent mainly lies between 1.5 and 3.5, while the disc base density of $\log \rho_0 \approx -12$ is the most probable to be found among Be

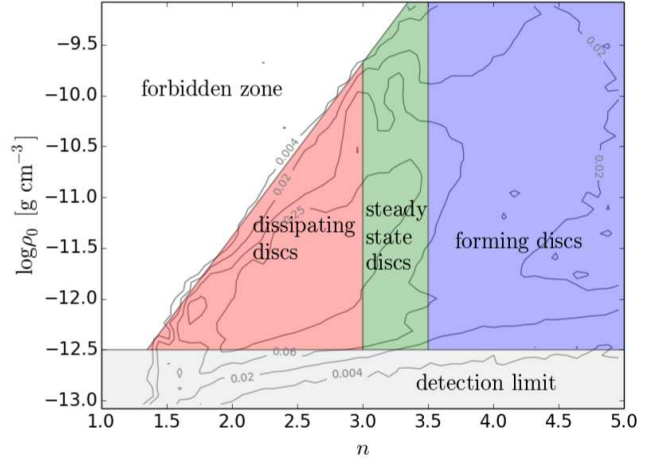


Figure 13. Typical regions for distinct disc dynamical states in the $n - \log \rho_0$ diagram, according to VDD hydrodynamical simulations. The defined regions were superimposed on the combined `emcee` posterior distributions for our sample (see Figure 7).

discs. The disc base densities typically range from this lower limit up to $\log \rho_0 \approx -10$, and we observe a positive correlation between n and $\log \rho_0$. Such results are in agreement with those found by Waters et al. (1987).

Denser discs are more likely to occur around earlier-type Be stars, which either means that more massive objects can provide higher mass injection rates to the disc, or hotter objects have smaller α . This question requires further investigation. No clear correlation was found between n and T_{eff} .

The disc mass decretion rates were estimated for our sample under the approximation of a steady-state disc. The values for $\dot{M}_{\text{SS}}/\alpha$ range from 10^{-12} to $10^{-8} M_{\odot} \text{ yr}^{-1}$, and they increase with the stellar luminosity. These results are up to three orders of magnitude smaller than those found by Waters et al. (1987), since the VDD outflow velocities are much smaller than their outflowing wind model. Additionally, our results do not show a mass-loss transition at $\log(L_{\star}/L_{\odot}) = 3$, as suggested by those authors. Finally, our results are compatible with the mass decretion rates found by Granada et al. (2013), which were based on stellar evolution arguments.

The dynamical scenario predicted by the time-dependent VDD model provides a satisfactory interpretation key for the results from the SED fitting. Evolutionary tracks on the $n - \log \rho_0$ diagram suggest that most of the observed cases correspond to dissipating discs, since this evolutionary stage has a much longer time scale than the disc formation stage. The hydrodynamical interpretation of our results leads to the classification of distinct regions of the $n - \log \rho_0$ plane, associated with different evolutionary stages. The $n \lesssim 3$ region is associated with flatter SED slopes and dissipating discs; the strip between $n \approx 3$ and $n \approx 3.5$ corresponds to the steady-state zone; finally, forming discs occupy the region where $n \gtrsim 3.5$. The more extended region for the steady-state rather than the canonical $n = 3.5$ may be due to disc non-isothermality and/or non-isoviscosity. The smaller number of solutions around the steady-state region suggests the discs spend less time being actively fed than passively

dissipating, which means that mass injection episodes must be shorter when compared to the dissipation time. Studies with a denser time coverage are required in order to impose better constraints on such time scales.

ACKNOWLEDGMENTS

We thank the anonymous referee for the useful comments. This work made use of the computing facilities of the Laboratory of Astroinformatics (IAG/USP, NAT/Unicsul), whose purchase was made possible by the Brazilian agency FAPESP (grant 2009/54006-4) and the INCT-A. R. G. V. acknowledges the support from FAPESP (grant 2012/20364-4), A. C. C. acknowledges support from CNPq (grant 307594/2015-7) and FAPESP (grant 2015/17967-7), J. E. B. acknowledges support from the NSF (grant AST-1412135).

REFERENCES

- Bjorkman, J. E., & Carciofi, A. C. 2005, in *Astronomical Society of the Pacific Conference Series*, Vol. 337, *The Nature and Evolution of Disks Around Hot Stars*, ed. R. Ignace & K. G. Gayley, 75
- Brussaard, P. J., & van de Hulst, H. C. 1962, *Reviews of Modern Physics*, 34, 507
- Carciofi, A. C. 2011, in *IAU Symposium*, Vol. 272, *IAU Symposium*, ed. C. Neiner, G. Wade, G. Meynet, & G. Peters, 325–336
- Carciofi, A. C., & Bjorkman, J. E. 2006, *ApJ*, 639, 1081
- Carciofi, A. C., & Bjorkman, J. E. 2008, *ApJ*, 684, 1374
- Carciofi, A. C., Miroschnichenko, A. S., Kusakin, A. V., et al. 2006, *ApJ*, 652, 1617
- Carciofi, A. C., Okazaki, A. T., Le Bouquin, J.-B., et al. 2009, *A&A*, 504, 915
- Carciofi, A. C., Bjorkman, J. E., Otero, S. A., et al. 2012, *ApJ*, 744, L15
- Castelli, F., & Kurucz, R. L. 2003, in *IAU Symposium*, Vol. 210, *Modelling of Stellar Atmospheres*, ed. N. Piskunov, W. W. Weiss, & D. F. Gray, A20
- Cranmer, S. R. 1996, PhD thesis, Bartol Research Institute, University of Delaware
- Delaa, O., Stee, P., Meilland, A., et al. 2011, *A&A*, 529, A87
- Dougherty, S. M., & Taylor, A. R. 1992, *Nature*, 359, 808
- Ekström, S., Meynet, G., Maeder, A., & Barblan, F. 2008, *A&A*, 478, 467
- Espinosa Lara, F., & Rieutord, M. 2011, *A&A*, 533, A43
- Faes, D. M., Carciofi, A. C., A., D., et al. in preparation
- Foreman-Mackey, D., Hogg, D. W., Lang, D., & Goodman, J. 2013, *PASP*, 125, 306
- Frémat, Y., Zorec, J., Hubert, A.-M., & Floquet, M. 2005, *A&A*, 440, 305
- Georgy, C., Ekström, S., Granada, A., et al. 2013, *A&A*, 553, A24
- Granada, A., Ekström, S., Georgy, C., et al. 2013, *A&A*, 553, A25
- Hanuschik, R. W. 1996, *A&A*, 308, 170
- Haubois, X., Carciofi, A. C., Rivinius, T., Okazaki, A. T., & Bjorkman, J. E. 2012, *ApJ*, 756, 156
- Haubois, X., Mota, B. C., Carciofi, A. C., et al. 2014, *ApJ*, 785, 12
- Huat, A.-L., Hubert, A.-M., Baudin, F., et al. 2009, *A&A*, 506, 95
- Ishihara, D., Onaka, T., Kataza, H., et al. 2010, *A&A*, 514, A1
- Jones, C. E., Tycner, C., Sigut, T. A. A., Benson, J. A., & Hutter, D. J. 2008, *ApJ*, 687, 598
- Klement, R., Carciofi, A. C., Rivinius, T., et al. 2015, *A&A*, 584, A85
- Koubský, P., Kotková, L., Votruba, V., Šlechta, M., & Dvořáková, Š. 2012, *A&A*, 545, A121
- Krtićka, J., Owocki, S. P., & Meynet, G. 2011, *A&A*, 527, A84
- Lee, U., Osaki, Y., & Saio, H. 1991, *MNRAS*, 250, 432
- Meilland, A., Millour, F., Kanaan, S., et al. 2012, *A&A*, 538, A110
- Neugebauer, G., Habing, H. J., van Duinen, R., et al. 1984, *ApJ*, 278, L1
- Okazaki, A. T. 2001, *PASJ*, 53, 119
- Okazaki, A. T. 2007, in *Astronomical Society of the Pacific Conference Series*, Vol. 361, *Active OB-Stars: Laboratories for Stellar and Circumstellar Physics*, ed. A. T. Okazaki, S. P. Owocki, & S. Stefl, 230
- Okazaki, A. T., Bate, M. R., Ogilvie, G. I., & Pringle, J. E. 2002, *MNRAS*, 337, 967
- Oktariani, F., Okazaki, A. T., Kunjaya, C., & Aprilia. 2016, *MNRAS*, 459, 4440
- Panoglou, D., Carciofi, A. C., Vieira, R. G., et al. 2016, *MNRAS*, 461, 2616
- Porter, J. M. 1996, *MNRAS*, 280, L31
- Quirrenbach, A., Bjorkman, K. S., Bjorkman, J. E., et al. 1997, *ApJ*, 479, 477
- Rivinius, T., Baade, D., Stefl, S., et al. 1998, *A&A*, 333, 125
- Rivinius, T., & Štefl, S. 2000, in *Astronomical Society of the Pacific Conference Series*, Vol. 214, *IAU Colloq. 175: The Be Phenomenon in Early-Type Stars*, ed. M. A. Smith, H. F. Henrichs, & J. Fabregat, 581
- Rivinius, T., Štefl, S., & Baade, D. 2006, *A&A*, 459, 137
- Rivinius, T., Carciofi, A. C., & Martayan, C. 2013, *A&A Rev.*, 21, 69
- Shakura, N. I., & Sunyaev, R. A. 1973, *A&A*, 24, 337
- Sigut, T. A. A., & Jones, C. E. 2007, *ApJ*, 668, 481
- Silaj, J., Jones, C. E., Tycner, C., Sigut, T. A. A., & Smith, A. D. 2010, *ApJS*, 187, 228
- Snow, Jr., T. P. 1981, *ApJ*, 251, 139
- Stee, P., de Araujo, F. X., Vakili, F., et al. 1995, *A&A*, 300, 219
- Struve, O. 1931, *ApJ*, 73, 94
- Touhami, Y., Gies, D. R., Schaefer, G. H., et al. 2013, *ApJ*, 768, 128
- Townsend, R. H. D., Owocki, S. P., & Howarth, I. D. 2004, *MNRAS*, 350, 189
- Tycner, C., Lester, J. B., Hajian, A. R., et al. 2005, *ApJ*, 624, 359
- Tycner, C., Jones, C. E., Sigut, T. A. A., et al. 2008, *ApJ*, 689, 461
- Vieira, R. G., Carciofi, A. C., & Bjorkman, J. E. 2015, *MNRAS*, 454, 2107
- von Zeipel, H. 1924, *MNRAS*, 84, 684
- Waters, L. B. F. M., Coté, J., & Lamers, H. J. G. L. M. 1987, *A&A*, 185, 206
- Wood, K., Bjorkman, K. S., & Bjorkman, J. E. 1997, *ApJ*, 477, 926
- Wright, E. L., Eisenhardt, P. R. M., Mainzer, A. K., et al. 2010, *AJ*, 140, 1868

APPENDIX A: SELECTED SAMPLE

Table E1 lists the selected Be stars from Frémat et al.'s sample, their respective spectral classification and color-corrected fluxes (see Section 3).

APPENDIX B: COMPUTING THE STELLAR PARAMETERS

Frémat et al. (2005) derived the fundamental parameters of 130 B-type stars, based on the fit of their optical spectra.

These authors made a distinction between *apparent* parameters, where the rotation effects are neglected, and *parent non-rotating counterpart* (pnrc) parameters, which span a family of models of different rotation velocities. In this work, we adopted the pnrc parameters to compute our SED models. However, they have first to be converted to the fundamental parameters of a specific rotation rate. The pnrc parameters are $T_{\text{eff},0}$, $\log g_0$, the true $v \sin i$, the critical velocity V_c and the inclination i , while the rotating stellar parameters necessary for the pseudo-photosphere model are the rotation rate $\omega = \Omega/\Omega_{\text{crit}}$ (which is equivalent to W , see Rivinius et al. 2013), M_\star , R_{pole} and L_\star . In this appendix, we derive the expressions needed to convert the pnrc parameters into the rotating model parameters of interest. By evaluating Equation (2) from Frémat et al. (2005) at $\omega = 1$, we have:

$$R_{\text{pole}}(\omega = 1) = R_0[1 - 0.0152 P(M_\star)], \quad (\text{B1})$$

where R_0 is the radius of the non-rotating star, and

$$P(M_\star) = 5.66 + \frac{9.43}{(M_\star/M_\odot)^2} \quad (M_\star/M_\odot \gtrsim 2). \quad (\text{B2})$$

The rotational critical velocity is given by (e.g., Rivinius et al. 2013)

$$V_c^2 = \frac{2}{3} \frac{GM_\star}{R_{\text{pole}}|_{\omega=1}} = \frac{2}{3} \frac{GM_\star}{R_0[1 - 0.0152 P(M_\star)]}, \quad (\text{B3})$$

and the stellar mass can be written as

$$M_\star = \frac{g_0 R_0^2}{G}. \quad (\text{B4})$$

By using these definitions in Equation (B1), we find an equation for R_0 :

$$R_0 = \frac{3}{2} \frac{V_c^2}{g_0} \left[1 - 0.0152 P \left(\frac{g_0 R_0^2}{G} \right) \right], \quad (\text{B5})$$

which can be numerically solved. Once R_0 is known, we can compute R_{pole} from Equation (B1), and use Equation (1) from Frémat et al. (2005) to derive an expression for the equatorial radius:

$$\frac{R_{\text{eq}}/R_0}{1 - P(M_\star) \bar{\tau}} = 1 + \frac{\omega^2}{2} \left[\frac{R_{\text{eq}}/(1.5 R_0)}{1 - 0.0152 P(M_\star)} \right]^3, \quad (\text{B6})$$

where

$$\omega = \cos \left\{ 3 \left[\cos^{-1} \left(\frac{v_{\text{rot}}}{2V_c} \right) - \pi \right] \right\} \quad (\text{B7})$$

(e.g., Rivinius et al. 2013),

$$\bar{\tau} \simeq (0.0072 + 0.008\eta^{1/2})\eta^{1/2}, \quad (\text{B8})$$

and

$$\eta = \omega^2 \left\{ \frac{R_{\text{eq}}}{1.5 R_0 [1 - 0.0152 P(M_\star)]} \right\}^3. \quad (\text{B9})$$

Finally, the luminosity can be computed by:

$$L_\star = L_0 \left[\bar{a} + (1 - \bar{a}) e^{-\bar{b}\bar{\tau}} \right], \quad (\text{B10})$$

where

$$L_0 = 4\pi R_0^2 \sigma_B T_{\text{eff},0}^4, \quad (\text{B11})$$

$$\bar{a} = 0.675 + 0.046 \left(\frac{M_\star}{M_\odot} \right)^{1/2}, \quad (\text{B12})$$

$$\bar{b} = 52.71 + 20.63 \left(\frac{M_\star}{M_\odot} \right)^{1/2}. \quad (\text{B13})$$

APPENDIX C: MCMC RESULTS

Table E2 presents the stellar and disc parameters derived with the `emcee` code. The parameter values correspond to the median of the sampled distributions, and the derived uncertainties correspond to a 1- σ confidence interval (see Section 4.1).

APPENDIX D: EFFECTIVE RADII AND DISC TRUNCATION EFFECTS

The disc effective radius is a function of wavelength, and thus has a particular value at each IR bandpass adopted for this work. The interested reader can easily compute it using the following expression:

$$\frac{\bar{R}}{R_{\text{eq}}} = \left[1.33 \times 10^{-3} \left(\frac{T_{\text{eff}}}{10^4 \text{ K}} \right)^{-1} \left(\frac{R_{\text{eq}}}{R_\odot} \right)^{3/2} \left(\frac{M_\star}{M_\odot} \right)^{-1/2} \right. \quad (\text{D1})$$

$$\left. \times \left(\frac{\rho_0}{10^{-12} \text{ g cm}^{-2}} \right)^2 \lambda_{\mu\text{m}}^2 (g_{\text{ff}} + g_{\text{bf}}) \right]^{1/(2n-\beta)}, \quad (\text{D2})$$

where the same assumptions described in Section 4 were adopted. Figure E1 shows the \bar{R} distribution for the shortest and the longest wavelengths used in this work. Although the $\bar{R}/R_{\text{eq}} < 1$ cases have no geometrical interpretation, they still remain useful for providing information about the disc vertical optical depth scale (Vieira et al. 2015). We see that $\bar{R}/R_{\text{eq}} < 10$ for practically all the sample (except for HD 41335 and HD 110432 at $60 \mu\text{m}$).

Disc truncation caused by a binary companion may be of importance for the SED if it disrupts the pseudo-photosphere at the wavelength of interest. The main result of disc truncation is a discontinuity in the SED first derivative at $\bar{\lambda}$ such that $\bar{R}(\bar{\lambda}) = R_t$, where R_t is the truncation radius (Vieira et al. 2015; see also Fig. 27 in Panoglou et al. 2016). At $\lambda > \bar{\lambda}$, the SED slope becomes equal to the photospheric one.

It follows that the results presented in this paper can potentially be affected by the presence of unknown binaries if the truncation radius is $R_t \lesssim 10 R_{\text{eq}}$.

However, according to the work of Panoglou et al. (2016) such a small truncation radius would be associated to short-period binaries ($P < 20$ days). The shortest known orbital periods in our sample are the Be+sdO systems *o* Puppis (Koubský et al. 2012) and 59 Cyg (Rivinius & Štefl 2000), both having $P \approx 30$ days. Although the existence of an undetected companion so close to the Be cannot be discarded, it is probably unlikely to find such a dramatic case in the sample. The lack of evidence of disc truncation at relatively small radii is another hint that close binaries are not common among Be stars, and therefore binarity is probably not relevant for the ejection and formation of discs.

APPENDIX E: SED EVOLUTION

The code `SINGLEBE` (Okazaki 2007; Okazaki et al. 2002) computes the one-dimensional time evolution of the radial density profile of a decretion disc. Mass is injected into orbit above the base of the disc at $1.04 R_{\text{eq}}$, and the disc is assumed to be azimuthally symmetric. Since this mass injection is the source of the angular momentum carried away by the decretion disc, most of the injected mass falls back onto the star. Typically, the decretion rate of the disc, \dot{M}_{SS} , is two orders of magnitude smaller than the injection rate. Given the disc density profile, the free-free and bound-free LTE opacities can be written as (Brussaard & van de Hulst 1962)

$$\kappa_{\lambda} = 3.692 \times 10^8 [1 - \exp(-hc/\lambda k T_{\text{d}})] \bar{z}^2 T_{\text{d}}^{-1/2} \times (\lambda/c)^3 \gamma (\rho/\mu m_{\text{H}})^2 [g_{\text{ff}}(\lambda, T_{\text{d}}) + g_{\text{bf}}(\lambda, T_{\text{d}})], \quad (\text{E1})$$

where we again use the isothermal approximation (see Section 2). For simplicity, we restrict our discussion of the SED evolution to the pole-on case. The vertical optical depth is given by

$$\tau_z = \int_{-\infty}^{+\infty} \kappa_{\lambda} dz = \tau_0 \frac{H(\varpi)}{H_0} \left[\frac{\rho(\varpi, z=0)}{\rho_0} \right]^2, \quad (\text{E2})$$

where $H(\varpi)/H_0 = \varpi^{3/2}$ is the isothermal scale height, and

$$\tau_0 = \sqrt{\pi} H_0 \kappa_{\lambda}(\varpi = R_{\text{eq}}, z = 0). \quad (\text{E3})$$

The specific intensity can be expressed as

$$I_{\lambda}(\varpi) = \begin{cases} S_{\lambda}^*(T_{\text{eff}}) & (\varpi \leq R_{\text{eq}}) \\ B_{\lambda}(T_{\text{d}}) [1 - \exp(-\tau_z)] & (R_{\text{eq}} < \varpi \leq R_{\text{d}}), \end{cases} \quad (\text{E4})$$

and consequently the total flux can be expressed by

$$F_{\lambda} = \frac{1}{d^2} \int_0^{R_{\text{d}}} I_{\lambda}(\varpi) 2\pi \varpi d\varpi. \quad (\text{E5})$$

Figure E2 shows the evolution of both the disc radial density profile and the IR SED for some dynamical scenarios of interest. The SED excess responds very quickly to the disc formation, affecting the entire IR wavelength range within a few weeks (upper panels). In contrast, the disc dissipation slowly modifies the SED with the excess decreasing first at shorter wavelengths (middle panels). Finally, the bottom panels show the case of periodic mass injection.

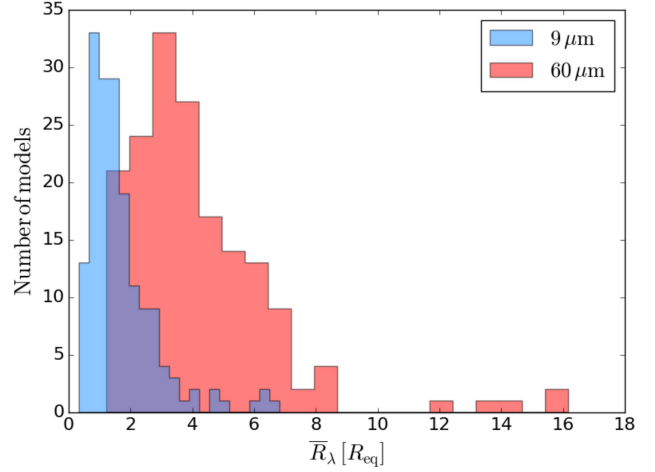


Figure E1. Distribution of derived \bar{R} values, computed at the shortest and longest wavelengths adopted in this work.

Table E1: Selected sample and respective color-corrected fluxes.

Name	HD	Spectral type ^a	IRAS			AKARI		WISE	
			12 μm [Jy]	25 μm [Jy]	60 μm [Jy]	9 μm [Jy]	18 μm [Jy]	12 μm [Jy]	22 μm [Jy]
γ Cas	5394	B0.5IVpe	14.9 \pm 1.1	6.7 \pm 0.7	2.2 \pm 0.5	28.7 \pm 0.1	13.02 \pm 0.04	–	–
ϕ And	6811	B5IIIe	0.8 \pm 0.1	0.4 \pm 0.1	–	–	–	–	–
HD 11606	11606	B2Vne	0.5 \pm 0.1	0.25 \pm 0.04	–	0.47 \pm 0.05	0.25 \pm 0.02	0.321 \pm 0.004	0.190 \pm 0.004
HD 18552	18552	B7IVe	–	–	–	0.32 \pm 0.01	0.17 \pm 0.01	0.215 \pm 0.003	0.123 \pm 0.003
HD 20336	20336	B2.5Vn(e)	–	–	–	1.6 \pm 0.1	0.75 \pm 0.01	1.28 \pm 0.01	0.75 \pm 0.01
HD 22780	22780	B7Vn	–	–	–	–	–	0.404 \pm 0.005	0.189 \pm 0.004
13 Tau	23016	B9Vne	–	–	–	–	–	0.150 \pm 0.002	0.048 \pm 0.002
23 Tau	23480	B6IVe	–	–	–	1.46 \pm 0.03	1.3 \pm 0.1	0.68 \pm 0.01	0.53 \pm 0.02
HD 23552	23552	B8V	–	–	–	0.38 \pm 0.02	0.23 \pm 0.02	0.225 \pm 0.003	0.127 \pm 0.003
η Tau	23630	B7III	3.4 \pm 0.2	1.7 \pm 0.2	–	4.3 \pm 0.1	2.0 \pm 0.1	3.3 \pm 0.1	1.52 \pm 0.03
V* X Per	24534	O9.5III	–	–	–	1.9 \pm 0.1	0.76 \pm 0.01	1.41 \pm 0.01	0.70 \pm 0.01
48 Per	25940	B3Ve	3.1 \pm 0.2	1.6 \pm 0.2	0.7 \pm 0.1	4.01 \pm 0.03	2.1 \pm 0.1	3.08 \pm 0.02	1.74 \pm 0.03
DU Eri	28497	B2(V)ne	0.8 \pm 0.1	0.4 \pm 0.1	–	0.86 \pm 0.03	0.38 \pm 0.04	0.74 \pm 0.01	0.34 \pm 0.01
11 Cam	32343	B3Ve	1.6 \pm 0.2	1.3 \pm 0.1	2.2 \pm 0.2	1.15 \pm 0.03	0.8 \pm 0.1	0.87 \pm 0.01	0.68 \pm 0.01
λ Eri	33328	B2IVne	–	–	–	–	–	0.72 \pm 0.01	0.30 \pm 0.01
ψ^1 Ori	35439	B1Vn	1.2 \pm 0.1	0.5 \pm 0.1	–	1.6 \pm 0.1	0.68 \pm 0.04	1.45 \pm 0.02	0.68 \pm 0.01
120 Tau	36576	B2IV-Ve	1.1 \pm 0.1	0.9 \pm 0.3	1.3 \pm 0.2	1.75 \pm 0.03	1.12 \pm 0.03	1.25 \pm 0.01	0.82 \pm 0.02
HD 37657	37657	B3Vne	–	–	–	0.37 \pm 0.02	0.19 \pm 0.01	0.118 \pm 0.002	0.090 \pm 0.002
α Col	37795	B9Ve	4.7 \pm 0.2	2.3 \pm 0.2	0.9 \pm 0.1	5.16 \pm 0.02	2.58 \pm 0.02	3.92 \pm 0.04	2.18 \pm 0.03
HD 37967	37967	B2.5Ve	–	–	–	0.87 \pm 0.01	0.469 \pm 0.001	0.61 \pm 0.01	0.38 \pm 0.01
V* V1165 Tau	38010	B1Vpe	0.6 \pm 0.1	0.5 \pm 0.1	–	0.70 \pm 0.04	0.46 \pm 0.05	0.46 \pm 0.01	0.28 \pm 0.01
HD 40978	40978	B3Ve	–	–	–	–	–	0.164 \pm 0.002	0.089 \pm 0.002
HD 41335	41335	B3/5Vnne	1.8 \pm 0.2	0.9 \pm 0.1	–	–	–	1.47 \pm 0.02	0.77 \pm 0.01
HD 44458	44458	B1.5IVe	1.4 \pm 0.2	0.7 \pm 0.1	–	1.40 \pm 0.05	0.7 \pm 0.1	0.83 \pm 0.01	0.50 \pm 0.01
HD 45995	45995	B1.5Vne	–	–	–	0.75 \pm 0.01	0.3 \pm 0.1	0.390 \pm 0.005	0.237 \pm 0.005
HD 47054	47054	B8IVe	–	–	–	0.45 \pm 0.03	0.3 \pm 0.1	0.325 \pm 0.004	0.181 \pm 0.004
κ CMa	50013	B1.5Ve	5.2 \pm 0.4	2.4 \pm 0.2	0.8 \pm 0.1	5.4 \pm 0.2	2.5 \pm 0.1	5.33 \pm 0.02	2.48 \pm 0.03
ω CMa	56139	B2IV-Ve	1.5 \pm 0.2	0.7 \pm 0.1	0.4 \pm 0.1	2.7 \pm 0.3	1.7 \pm 0.2	1.88 \pm 0.01	0.88 \pm 0.01
HD 58050	58050	B2Ve	–	–	–	–	–	0.046 \pm 0.001	0.017 \pm 0.001
HD 58343	58343	B2Vne	1.0 \pm 0.1	0.6 \pm 0.1	–	–	–	0.41 \pm 0.01	0.30 \pm 0.01
β CMi	58715	B8Ve	3.2 \pm 0.2	1.5 \pm 0.2	0.6 \pm 0.1	4.44 \pm 0.01	2.1 \pm 0.1	3.16 \pm 0.03	1.60 \pm 0.02
HD 58978	58978	B0.5IVe	0.7 \pm 0.1	0.24 \pm 0.04	–	–	–	0.225 \pm 0.003	0.108 \pm 0.003
HR 2911	60606	B2Vne	1.2 \pm 0.2	0.7 \pm 0.1	0.7 \pm 0.1	1.05 \pm 0.02	0.71 \pm 0.04	0.74 \pm 0.01	0.45 \pm 0.01
HD 60848	60848	O8:V:	–	–	–	–	–	0.100 \pm 0.001	0.049 \pm 0.002
o Pup	63462	B1IVe	2.0 \pm 0.2	0.7 \pm 0.1	–	–	–	1.81 \pm 0.02	0.72 \pm 0.01
HD 65875	65875	B2.5Ve	–	–	–	0.51 \pm 0.02	0.28 \pm 0.01	0.38 \pm 0.01	0.229 \pm 0.005
HR 3237	68980	B2ne	1.7 \pm 0.1	1.0 \pm 0.1	1.0 \pm 0.1	1.91 \pm 0.05	0.99 \pm 0.02	1.39 \pm 0.02	0.75 \pm 0.01
HR 3498	75311	B3V(n)	0.6 \pm 0.1	0.3 \pm 0.1	0.22 \pm 0.04	0.6 \pm 0.1	0.32 \pm 0.03	0.50 \pm 0.01	0.203 \pm 0.004
HR 3593	77320	B2Vnn(e)	–	–	–	0.33 \pm 0.04	0.105 \pm 0.005	0.317 \pm 0.004	0.166 \pm 0.004
HR 3858	83953	B5V	1.6 \pm 0.2	0.9 \pm 0.1	0.4 \pm 0.2	–	–	1.09 \pm 0.01	0.58 \pm 0.01

HD 86612	86612	B5Ve	–	–	–	0.60 ± 0.04	0.36 ± 0.03	0.44 ± 0.01	0.27 ± 0.01
HD 88661	88661	B5Vne	0.8 ± 0.1	0.5 ± 0.1	–	1.05 ± 0.01	0.58 ± 0.02	0.82 ± 0.01	0.52 ± 0.01
ω Car	89080	B8IIIe	2.4 ± 0.2	1.1 ± 0.1	0.50 ± 0.05	3.13 ± 0.02	1.41 ± 0.02	2.27 ± 0.01	1.12 ± 0.01
HD 91120	91120	B8/9IV/V	–	–	–	0.45 ± 0.03	0.22 ± 0.02	0.288 ± 0.003	0.143 ± 0.003
ρ Car	91465	B4Vne	5.5 ± 0.3	2.7 ± 0.2	–	7.0 ± 0.1	3.29 ± 0.02	7.7 ± 0.1	3.65 ± 0.05
δ Cen	105435	B2Vne	12.7 ± 0.9	7.1 ± 0.8	3.0 ± 0.4	13.3 ± 0.2	7.0 ± 0.1	11.8 ± 0.1	6.1 ± 0.1
HD 105521	105521	B3IVe	–	–	–	–	–	0.46 ± 0.01	0.217 ± 0.004
κ Dra	109387	B6IIIe	3.4 ± 0.2	1.7 ± 0.1	0.5 ± 0.1	4.06 ± 0.03	2.18 ± 0.04	2.83 ± 0.01	1.56 ± 0.02
HD 110432	110432	B0.5IVpe	3.8 ± 0.3	2.0 ± 0.3	–	5.25 ± 0.05	2.42 ± 0.03	3.88 ± 0.03	2.03 ± 0.03
λ Cru	112078	B3Vne	–	–	–	–	–	0.251 ± 0.003	0.076 ± 0.002
μ^2 Cru	112091	B5Vne	0.9 ± 0.1	0.6 ± 0.1	–	–	–	–	–
μ Cen	120324	B2Vnpe	–	–	–	4.7 ± 0.3	1.9 ± 0.1	0.89 ± 0.01	0.46 ± 0.01
HD 124367	124367	B4Vne	1.7 ± 0.3	0.8 ± 0.1	–	1.69 ± 0.02	0.96 ± 0.03	1.25 ± 0.02	0.81 ± 0.01
η Cen	127972	B2Ve	–	–	–	9.2 ± 0.6	4.4 ± 0.1	4.47 ± 0.03	2.39 ± 0.03
θ Cir	131492	B2IV/V	–	–	–	0.8 ± 0.1	0.34 ± 0.04	0.77 ± 0.01	0.32 ± 0.01
μ Lup	135734	B8Ve	0.9 ± 0.1	0.4 ± 0.1	0.3 ± 0.1	1.25 ± 0.03	0.62 ± 0.01	0.81 ± 0.01	0.41 ± 0.01
χ Oph	148184	B2Vne	8.8 ± 0.8	4.5 ± 0.6	2.3 ± 0.4	12.911 ± 0.002	6.45 ± 0.05	10.9 ± 0.2	5.5 ± 0.1
ζ Oph	149757	O9.2IV	–	–	–	4.0 ± 0.1	1.06 ± 0.04	2.38 ± 0.03	0.78 ± 0.02
ι Ara	157042	B2(V)nne	1.1 ± 0.1	0.6 ± 0.1	–	1.16 ± 0.03	0.53 ± 0.04	0.83 ± 0.01	0.43 ± 0.01
α Ara	158427	B2Vne	10.3 ± 0.7	4.9 ± 0.5	1.7 ± 0.2	–	–	10.8 ± 0.2	5.65 ± 0.05
66 Oph	164284	B2Ve	2.9 ± 0.2	1.6 ± 0.2	0.8 ± 0.1	–	–	–	–
λ Pav	173948	B2Ve	–	–	–	–	–	0.40 ± 0.01	0.124 ± 0.003
64 Ser	175869	B8/9II	–	–	–	–	–	0.299 ± 0.004	0.180 ± 0.004
β Cyg B	183914	B8Ve	–	–	–	–	–	0.39 ± 0.01	0.142 ± 0.002
11 Cyg	185037	B8Vne	–	–	–	–	–	0.196 ± 0.003	0.106 ± 0.003
12 Vul	187811	B2.5Ve	–	–	–	–	–	0.366 ± 0.005	0.131 ± 0.003
25 Cyg	189687	B3IVe	–	–	–	0.39 ± 0.01	0.26 ± 0.02	–	–
28 Cyg	191610	B2.5Ve	1.0 ± 0.1	0.5 ± 0.1	–	0.40 ± 0.02	0.17 ± 0.05	0.277 ± 0.004	0.132 ± 0.003
20 Vul	192044	B7Ve	–	–	–	0.36 ± 0.02	0.15 ± 0.01	0.252 ± 0.003	0.141 ± 0.004
25 Vul	193911	B6IVe	0.4 ± 0.1	0.22 ± 0.05	–	–	–	–	–
HD 194335	194335	B2IIIe	–	–	–	0.45 ± 0.01	0.3 ± 0.1	0.350 ± 0.005	0.165 ± 0.004
59 Cyg	200120	B1.5Vnne	–	–	–	2.5 ± 0.1	0.95 ± 0.04	1.46 ± 0.02	0.60 ± 0.01
6 Cep	203467	B3IVe	–	–	–	2.52 ± 0.05	2.4 ± 0.1	1.80 ± 0.02	1.93 ± 0.03
HD 208682	208682	B2Ve	0.4 ± 0.1	0.30 ± 0.05	–	–	–	–	–
η PsA	209014	B8/9V+B8/9	–	–	–	0.507 ± 0.001	0.23 ± 0.03	0.337 ± 0.004	0.182 ± 0.005
31 Peg	212076	B2IV-Ve	–	–	–	2.08 ± 0.03	0.99 ± 0.02	0.81 ± 0.01	0.60 ± 0.01
π Aqr	212571	B1III-IVe	–	–	–	–	–	0.72 ± 0.01	0.31 ± 0.01
ϵ PsA	214748	B8Ve	0.9 ± 0.1	0.4 ± 0.1	–	1.15 ± 0.01	0.52 ± 0.01	0.81 ± 0.01	0.43 ± 0.01
β Psc	217891	B6Ve	0.6 ± 0.1	0.4 ± 0.1	0.3 ± 0.1	1.5 ± 0.2	0.7 ± 0.1	1.48 ± 0.02	0.85 ± 0.01
HD 224559	224559	B4Vne	–	–	–	0.42 ± 0.02	0.184 ± 0.003	0.311 ± 0.004	0.197 ± 0.004

(a) Spectral classification provided by SIMBAD Astronomical Database⁴⁴ <http://simbad.u-strasbg.fr/simbad/>

Table E2: Stellar and disc parameters sampled with the `emcee` code.

HD					IRAS			AKARI			WISE		
	M_{\star} [M_{\odot}]	R_{pole} [R_{\odot}]	$\log L_{\star}$ [L_{\odot}]	W	n	$\log \rho_0$ [g cm^{-3}]	$\log(\dot{M}_{\text{SS}}/\alpha)$ [$M_{\odot} \text{ yr}^{-1}$]	n	$\log \rho_0$ [g cm^{-3}]	$\log(\dot{M}_{\text{SS}}/\alpha)$ [$M_{\odot} \text{ yr}^{-1}$]	n	$\log \rho_0$ [g cm^{-3}]	$\log(\dot{M}_{\text{SS}}/\alpha)$ [$M_{\odot} \text{ yr}^{-1}$]
5394	25 ± 9	8 ± 2	4.7 ± 0.3	0.9 ± 0.1	3.8 ^{+0.9} _{-0.6}	-10.8 ^{+0.6} _{-0.5}	-9.6	3.29 ^{+0.05} _{-0.05}	-10.9 ^{+0.4} _{-0.3}	-9.7	–	–	–
6811	5.6 ± 1.0	10 ± 1	3.3 ± 0.1	0.6 ± 0.2	5 ⁺¹² ₋₂	-12.4 ^{+1.2} _{-0.3}	-10.9	–	–	–	–	–	–
11606	9 ± 2	6.2 ± 0.6	3.9 ± 0.1	0.7 ± 0.1	4 ⁺⁹ ₋₁	-11.6 ^{+3.1} _{-0.6}	-10.6	2.8 ^{+1.5} _{-0.6}	-12.0 ^{+0.5} _{-0.2}	-11.0	2.3 ^{+0.1} _{-0.2}	-12.2 ^{+0.1} _{-0.1}	-11.2
18552	3.9 ± 0.4	3.9 ± 0.2	2.78 ± 0.05	0.80 ± 0.05	–	–	–	2.1 ^{+0.3} _{-0.2}	-12.3 ^{+0.1} _{-0.2}	-11.6	2.1 ^{+0.1} _{-0.1}	-12.4 ^{+0.1} _{-0.1}	-11.7
20336	7 ± 1	3.9 ± 0.4	3.4 ± 0.1	0.7 ± 0.1	–	–	–	3.3 ^{+0.3} _{-0.2}	-10.8 ^{+0.3} _{-0.3}	-10.3	2.6 ^{+0.1} _{-0.1}	-11.2 ^{+0.1} _{-0.1}	-10.8
22780	6.4 ± 0.8	6.5 ± 0.5	3.3 ± 0.1	0.8 ± 0.1	–	–	–	–	–	–	2.5 ^{+0.3} _{-0.3}	-12.3 ^{+0.2} _{-0.2}	-11.2
23016	3.5 ± 0.6	2.7 ± 0.3	2.3 ± 0.1	0.7 ± 0.1	–	–	–	–	–	–	9 ⁺⁵ ₋₃	-11.4 ^{+1.0} _{-0.7}	-11.4
23480	3.8 ± 0.6	3.5 ± 0.3	2.7 ± 0.1	0.8 ± 0.1	–	–	–	2.0 ^{+0.2} _{-0.1}	-12.1 ^{+0.1} _{-0.1}	-11.6	2.0 ^{+0.1} _{-0.1}	-12.2 ^{+0.1} _{-0.1}	-11.8
23552	4.5 ± 0.7	3.9 ± 0.4	2.7 ± 0.1	0.7 ± 0.1	–	–	–	2.4 ^{+0.4} _{-0.3}	-11.9 ^{+0.2} _{-0.2}	-11.4	2.5 ^{+0.1} _{-0.1}	-11.9 ^{+0.2} _{-0.2}	-11.5
23630	5 ± 1	9 ± 1	3.3 ± 0.1	0.8 ± 0.1	4 ⁺⁴ ₋₁	-12.3 ^{+0.9} _{-0.3}	-10.6	2.9 ^{+0.2} _{-0.3}	-12.3 ^{+0.2} _{-0.1}	-10.6	3.2 ^{+0.2} _{-0.3}	-12.3 ^{+0.3} _{-0.2}	-10.7
24534	11 ± 2	6.1 ± 0.7	4.2 ± 0.1	0.7 ± 0.1	–	–	–	4.0 ^{+0.3} _{-0.2}	-10.3 ^{+0.4} _{-0.3}	-9.2	3.1 ^{+0.1} _{-0.1}	-10.9 ^{+0.3} _{-0.3}	-9.8
25940	5.5 ± 0.8	4.8 ± 0.5	3.3 ± 0.1	0.7 ± 0.2	2.9 ^{+0.2} _{-0.2}	-11.4 ^{+0.2} _{-0.2}	-10.6	2.8 ^{+0.1} _{-0.1}	-11.4 ^{+0.1} _{-0.1}	-10.7	2.7 ^{+0.1} _{-0.1}	-11.5 ^{+0.1} _{-0.1}	-10.7
28497	14 ± 4	4.7 ± 0.9	4.1 ± 0.2	0.7 ± 0.1	4 ⁺⁶ ₋₁	-10.3 ^{+3.3} _{-0.8}	-9.7	4.0 ^{+2.1} _{-0.8}	-10.5 ^{+0.9} _{-0.5}	-9.9	3.4 ^{+0.1} _{-0.1}	-10.7 ^{+0.3} _{-0.3}	-10.2
32343	6.1 ± 1.0	4.8 ± 0.6	3.1 ± 0.1	0.6 ± 0.2	1.7 ^{+0.1} _{-0.1}	-12.2 ^{+0.1} _{-0.1}	-11.7	2.2 ^{+0.2} _{-0.2}	-12.0 ^{+0.1} _{-0.1}	-11.4	2.0 ^{+0.1} _{-0.1}	-12.1 ^{+0.1} _{-0.1}	-11.5
33328	10 ± 1	7.4 ± 0.6	4.2 ± 0.1	0.8 ± 0.1	–	–	–	–	–	–	2.9 ^{+0.4} _{-0.4}	-12.2 ^{+0.3} _{-0.2}	-10.9
35439	11 ± 2	5.5 ± 0.5	3.9 ± 0.1	0.7 ± 0.1	6 ⁺¹¹ ₋₂	-10 ⁺⁴ ₋₁	-8.7	4.2 ^{+1.4} _{-0.7}	-10.6 ^{+0.6} _{-0.4}	-9.8	3.4 ^{+0.1} _{-0.1}	-11.0 ^{+0.3} _{-0.3}	-10.2
36576	11 ± 2	6.2 ± 0.6	4.1 ± 0.1	0.7 ± 0.1	1.7 ^{+0.1} _{-0.1}	-12.0 ^{+0.2} _{-0.2}	-11.0	2.3 ^{+0.1} _{-0.1}	-11.4 ^{+0.1} _{-0.1}	-10.4	2.36 ^{+0.04} _{-0.04}	-11.4 ^{+0.1} _{-0.1}	-10.4
37657	10 ± 1	7.1 ± 0.6	3.8 ± 0.1	0.7 ± 0.1	–	–	–	2.8 ^{+0.3} _{-0.3}	-11.8 ^{+0.3} _{-0.3}	-10.7	2.0 ^{+0.1} _{-0.1}	-12.2 ^{+0.1} _{-0.1}	-11.1
37795	5.7 ± 0.6	6.0 ± 0.4	3.0 ± 0.1	0.9 ± 0.1	2.9 ^{+0.2} _{-0.2}	-12.2 ^{+0.1} _{-0.1}	-11.1	2.5 ^{+0.1} _{-0.2}	-12.2 ^{+0.1} _{-0.1}	-11.2	2.5 ^{+0.2} _{-0.2}	-12.3 ^{+0.1} _{-0.1}	-11.3
37967	8 ± 2	5.0 ± 0.8	3.3 ± 0.1	0.7 ± 0.1	–	–	–	2.6 ^{+0.1} _{-0.1}	-11.8 ^{+0.2} _{-0.2}	-11.1	2.4 ^{+0.1} _{-0.1}	-11.8 ^{+0.2} _{-0.2}	-11.2
38010	13 ± 3	4.4 ± 0.7	4.0 ± 0.1	0.7 ± 0.1	2.3 ^{+1.3} _{-0.4}	-11.5 ^{+0.9} _{-0.4}	-10.9	2.4 ^{+0.5} _{-0.3}	-11.5 ^{+0.3} _{-0.4}	-10.9	2.5 ^{+0.1} _{-0.1}	-11.5 ^{+0.2} _{-0.2}	-11.0
40978	9 ± 2	7 ± 1	3.8 ± 0.1	0.7 ± 0.1	–	–	–	–	–	–	2.7 ^{+0.2} _{-0.2}	-12.0 ^{+0.3} _{-0.2}	-10.7
41335	8 ± 2	4.1 ± 0.7	3.6 ± 0.1	0.7 ± 0.1	3.4 ^{+1.4} _{-0.6}	-9.8 ^{+1.4} _{-0.7}	-9.2	–	–	–	3.0 ^{+0.1} _{-0.1}	-10.3 ^{+0.3} _{-0.3}	-9.8
44458	13 ± 3	8.4 ± 1.0	4.4 ± 0.1	0.7 ± 0.1	4 ⁺⁵ ₋₁	-11.0 ^{+2.0} _{-0.7}	-9.6	3.2 ^{+0.9} _{-0.4}	-11.7 ^{+0.4} _{-0.4}	-10.3	2.4 ^{+0.1} _{-0.1}	-12.0 ^{+0.2} _{-0.2}	-10.7
45995	10 ± 2	5.9 ± 0.6	3.9 ± 0.1	0.7 ± 0.1	–	–	–	6 ⁺⁵ ₋₂	-11.2 ^{+1.2} _{-0.8}	-10.2	2.4 ^{+0.1} _{-0.1}	-12.0 ^{+0.1} _{-0.1}	-11.1
47054	5.0 ± 0.8	5.3 ± 0.6	2.9 ± 0.1	0.7 ± 0.1	–	–	–	5 ⁺¹⁴ ₋₂	-11.8 ^{+2.1} _{-0.5}	-11.1	2.4 ^{+0.2} _{-0.2}	-12.3 ^{+0.2} _{-0.2}	-11.5

50013	12 ± 3	5.3 ± 1.0	4.0 ± 0.2	0.7 ± 0.2	$3.5^{+0.3}_{-0.3}$	$-10.7^{+0.4}_{-0.3}$	-9.9	$3.2^{+0.3}_{-0.2}$	$-11.0^{+0.3}_{-0.3}$	-10.2	$3.4^{+0.1}_{-0.1}$	$-10.8^{+0.3}_{-0.3}$	-10.0
56139	10 ± 4	8 ± 2	3.9 ± 0.2	0.6 ± 0.2	$3.2^{+0.8}_{-0.5}$	$-11.6^{+0.5}_{-0.4}$	-10.4	$3.2^{+3.1}_{-0.9}$	$-11.4^{+1.3}_{-0.5}$	-10.2	$3.3^{+0.1}_{-0.1}$	$-11.5^{+0.3}_{-0.3}$	-10.3
58050	10 ± 2	5.6 ± 0.9	3.6 ± 0.1	0.6 ± 0.2	-	-	-	-	-	-	6^{+3}_{-1}	-11^{+1}_{-1}	-10.1
58343	7 ± 1	6.5 ± 0.9	3.4 ± 0.1	0.5 ± 0.2	$2.8^{+2.8}_{-0.6}$	$-11.7^{+1.2}_{-0.4}$	-10.8	-	-	-	$2.1^{+0.1}_{-0.1}$	$-12.2^{+0.1}_{-0.1}$	-11.4
58715	3.9 ± 0.5	3.6 ± 0.3	2.5 ± 0.1	0.8 ± 0.1	$2.9^{+0.3}_{-0.3}$	$-12.1^{+0.2}_{-0.2}$	-11.7	$3.0^{+1.1}_{-0.3}$	$-12.1^{+0.1}_{-0.1}$	-11.7	$2.7^{+0.2}_{-0.2}$	$-12.1^{+0.1}_{-0.1}$	-11.8
58978	13 ± 3	4.5 ± 0.8	3.9 ± 0.1	0.7 ± 0.1	11^{+47}_{-6}	-7^{+23}_{-3}	-6.2	-	-	-	$3.1^{+0.2}_{-0.2}$	$-11.6^{+0.3}_{-0.3}$	-11.1
60606	9 ± 2	6.3 ± 0.7	3.7 ± 0.1	0.7 ± 0.1	$2.1^{+0.1}_{-0.1}$	$-11.8^{+0.2}_{-0.2}$	-10.8	$2.2^{+0.1}_{-0.1}$	$-11.8^{+0.1}_{-0.1}$	-10.8	$2.5^{+0.1}_{-0.1}$	$-11.7^{+0.1}_{-0.1}$	-10.8
60848	14 ± 3	5.5 ± 0.6	4.3 ± 0.1	0.7 ± 0.2	-	-	-	-	-	-	$3.0^{+0.2}_{-0.2}$	$-11.9^{+0.2}_{-0.2}$	-11.1
63462	20 ± 3	8.0 ± 0.8	4.7 ± 0.1	0.94 ± 0.06	6^{+6}_{-2}	-9^{+4}_{-1}	-7.5	-	-	-	$4.6^{+0.2}_{-0.2}$	$-10.1^{+0.3}_{-0.3}$	-8.7
65875	8 ± 2	5.2 ± 0.6	3.6 ± 0.1	0.7 ± 0.2	-	-	-	$2.7^{+0.2}_{-0.2}$	$-11.2^{+0.2}_{-0.2}$	-10.4	$2.5^{+0.1}_{-0.1}$	$-11.3^{+0.2}_{-0.2}$	-10.5
68980	13 ± 2	5.9 ± 0.6	4.1 ± 0.1	0.6 ± 0.2	$2.1^{+0.1}_{-0.1}$	$-11.8^{+0.1}_{-0.1}$	-11.0	$2.8^{+0.1}_{-0.1}$	$-11.5^{+0.1}_{-0.2}$	-10.7	$2.8^{+0.1}_{-0.1}$	$-11.5^{+0.1}_{-0.1}$	-10.7
75311	5 ± 1	3.3 ± 0.6	3.0 ± 0.1	0.7 ± 0.1	$2.3^{+0.2}_{-0.2}$	$-11.7^{+0.2}_{-0.2}$	-11.5	$3.0^{+5.0}_{-0.8}$	$-11.5^{+1.7}_{-0.5}$	-11.2	$4.3^{+0.3}_{-0.3}$	$-11.0^{+0.3}_{-0.4}$	-10.8
77320	9 ± 2	4.7 ± 0.9	3.6 ± 0.2	0.7 ± 0.1	-	-	-	10^{+14}_{-5}	-9^{+4}_{-2}	-8.7	$2.8^{+0.1}_{-0.2}$	$-11.6^{+0.3}_{-0.3}$	-11.1
83953	6.8 ± 1.0	5.3 ± 0.5	3.3 ± 0.1	0.7 ± 0.1	$2.8^{+0.7}_{-0.4}$	$-11.7^{+0.4}_{-0.2}$	-10.9	-	-	-	$2.6^{+0.1}_{-0.1}$	$-12.0^{+0.1}_{-0.1}$	-11.2
86612	5.3 ± 0.8	4.7 ± 0.5	3.3 ± 0.1	0.7 ± 0.1	-	-	-	$2.4^{+0.5}_{-0.3}$	$-12.0^{+0.2}_{-0.2}$	-11.2	$2.4^{+0.1}_{-0.1}$	$-12.0^{+0.1}_{-0.2}$	-11.2
88661	10 ± 2	4.9 ± 0.8	3.7 ± 0.1	0.7 ± 0.2	4^{+13}_{-2}	-10^{+6}_{-1}	-9.6	$2.7^{+0.1}_{-0.1}$	$-11.3^{+0.2}_{-0.2}$	-10.6	$2.5^{+0.1}_{-0.1}$	$-11.4^{+0.2}_{-0.2}$	-10.8
89080	4.0 ± 0.6	5.1 ± 0.5	2.8 ± 0.1	0.8 ± 0.1	$2.9^{+0.2}_{-0.2}$	$-11.8^{+0.2}_{-0.2}$	-10.9	$3.0^{+0.2}_{-0.2}$	$-11.7^{+0.2}_{-0.2}$	-10.8	$3.0^{+0.1}_{-0.1}$	$-11.8^{+0.2}_{-0.2}$	-10.9
91120	2.6 ± 0.4	2.1 ± 0.2	2.0 ± 0.1	0.74 ± 0.06	-	-	-	$3.5^{+1.3}_{-0.6}$	$-10.7^{+0.9}_{-0.4}$	-11.0	$3.1^{+0.1}_{-0.1}$	$-11.0^{+0.2}_{-0.2}$	-11.3
91465	7 ± 2	5.8 ± 1.0	3.6 ± 0.1	0.7 ± 0.1	$3.0^{+0.5}_{-0.3}$	$-11.1^{+0.4}_{-0.3}$	-10.1	$3.1^{+0.1}_{-0.1}$	$-11.0^{+0.2}_{-0.3}$	-10.0	$3.3^{+0.1}_{-0.1}$	$-10.7^{+0.3}_{-0.2}$	-9.7
105435	12 ± 2	5.7 ± 0.6	3.9 ± 0.1	0.7 ± 0.2	$2.8^{+0.2}_{-0.2}$	$-11.2^{+0.2}_{-0.2}$	-10.4	$2.8^{+0.1}_{-0.1}$	$-11.3^{+0.1}_{-0.1}$	-10.5	$3.0^{+0.1}_{-0.1}$	$-11.1^{+0.2}_{-0.1}$	-10.3
105521	10 ± 1	12.7 ± 1.0	4.1 ± 0.1	0.7 ± 0.2	-	-	-	-	-	-	$2.9^{+0.2}_{-0.4}$	$-12.4^{+0.1}_{-0.1}$	-10.5
109387	7 ± 1	6.9 ± 0.7	3.4 ± 0.1	0.52 ± 0.03	$3.2^{+0.3}_{-0.2}$	$-11.2^{+0.3}_{-0.2}$	-10.3	$2.5^{+0.1}_{-0.1}$	$-11.7^{+0.2}_{-0.2}$	-10.8	$2.6^{+0.1}_{-0.1}$	$-11.7^{+0.1}_{-0.2}$	-10.8
110432	9 ± 2	4.8 ± 0.6	3.8 ± 0.1	0.9 ± 0.1	$3.1^{+0.9}_{-0.5}$	$-10.0^{+1.0}_{-0.6}$	-9.1	$3.3^{+0.1}_{-0.1}$	$-9.9^{+0.2}_{-0.2}$	-9.0	$3.0^{+0.1}_{-0.1}$	$-10.2^{+0.2}_{-0.2}$	-9.3
112078	4.7 ± 0.5	2.5 ± 0.2	2.78 ± 0.07	0.7 ± 0.1	-	-	-	-	-	-	11^{+7}_{-5}	$-11.7^{+1.2}_{-0.5}$	-11.7
112091	7.9 ± 1.3	4.5 ± 0.4	3.6 ± 0.1	0.7 ± 0.2	$2.6^{+1.0}_{-0.5}$	$-12.2^{+0.2}_{-0.2}$	-11.5	-	-	-	-	-	-
120324	10 ± 2	5.3 ± 0.6	3.8 ± 0.1	0.7 ± 0.1	-	-	-	$4.2^{+1.2}_{-0.7}$	$-11.3^{+0.5}_{-0.3}$	-10.5	$2.6^{+0.2}_{-0.2}$	$-12.1^{+0.1}_{-0.1}$	-11.5
124367	6.3 ± 1.0	4.1 ± 0.4	3.3 ± 0.1	0.7 ± 0.1	5^{+11}_{-2}	-10^{+5}_{-1}	-9.7	$2.4^{+0.1}_{-0.1}$	$-11.8^{+0.1}_{-0.1}$	-11.2	$2.3^{+0.1}_{-0.1}$	$-11.9^{+0.1}_{-0.1}$	-11.3
127972	10 ± 2	5.2 ± 0.6	3.7 ± 0.1	0.7 ± 0.1	-	-	-	$3.1^{+0.4}_{-0.3}$	$-11.4^{+0.3}_{-0.2}$	-10.7	$2.7^{+0.1}_{-0.1}$	$-11.8^{+0.1}_{-0.2}$	-11.1
131492	10 ± 2	8.0 ± 0.8	3.9 ± 0.1	0.7 ± 0.2	-	-	-	8^{+22}_{-4}	-10^{+8}_{-1}	-8.7	$4.2^{+0.2}_{-0.2}$	$-11.1^{+0.2}_{-0.2}$	-9.8
135734	3.2 ± 0.8	2.7 ± 0.5	2.5 ± 0.2	0.7 ± 0.1	$2.4^{+0.3}_{-0.2}$	$-11.7^{+0.3}_{-0.3}$	-11.6	$2.8^{+0.2}_{-0.2}$	$-11.5^{+0.3}_{-0.3}$	-11.4	$2.9^{+0.2}_{-0.2}$	$-11.5^{+0.3}_{-0.3}$	-11.4

148184	21 ± 4	7.9 ± 1.2	4.6 ± 0.1	0.6 ± 0.2	$2.7^{+0.3}_{-0.2}$	$-11.6^{+0.2}_{-0.2}$	-10.5	$2.9^{+1.1}_{-0.1}$	$-11.5^{+0.2}_{-0.1}$	-10.4	$3.1^{+0.1}_{-0.1}$	$-11.3^{+0.2}_{-0.2}$	-10.3
149757	11 ± 2	4.9 ± 0.5	4.2 ± 0.1	0.7 ± 0.1	–	–	–	18^{+26}_{-7}	-8^{+5}_{-2}	-7.7	7^{+2}_{-1}	$-10.9^{+0.7}_{-0.6}$	-10.1
157042	8 ± 2	3.0 ± 0.6	3.4 ± 0.2	0.7 ± 0.1	$3.0^{+1.2}_{-0.5}$	$-10.6^{+1.0}_{-0.5}$	-10.4	$3.5^{+0.5}_{-0.4}$	$-10.4^{+0.4}_{-0.4}$	-10.3	$2.9^{+0.1}_{-0.1}$	$-10.8^{+0.2}_{-0.2}$	-10.6
158427	4.1 ± 0.6	2.3 ± 0.2	2.8 ± 0.1	0.9 ± 0.1	$3.3^{+0.3}_{-0.3}$	$-10.3^{+0.3}_{-0.3}$	-10.2	–	–	–	$2.9^{+0.1}_{-0.1}$	$-10.5^{+0.1}_{-0.1}$	-10.4
164284	10 ± 3	4.8 ± 0.9	3.7 ± 0.2	0.7 ± 0.1	$2.6^{+0.1}_{-0.1}$	$-11.3^{+0.2}_{-0.2}$	-10.6	–	–	–	–	–	–
173948	12 ± 2	9 ± 1	4.2 ± 0.1	0.7 ± 0.2	–	–	–	–	–	–	10^{+3}_{-3}	-11^{+1}_{-1}	-10.0
175869	4.6 ± 0.9	6.2 ± 0.7	3.0 ± 0.1	0.7 ± 0.1	–	–	–	–	–	–	$2.4^{+0.1}_{-0.1}$	$-12.1^{+0.1}_{-0.2}$	-11.1
183914	4.0 ± 0.4	3.6 ± 0.3	2.7 ± 0.1	0.7 ± 0.1	–	–	–	–	–	–	$4.5^{+0.7}_{-0.9}$	$-12.1^{+0.3}_{-0.2}$	-11.6
185037	3.9 ± 0.7	3.0 ± 0.4	2.4 ± 0.1	0.7 ± 0.1	–	–	–	–	–	–	$2.5^{+0.2}_{-0.2}$	$-12.0^{+0.2}_{-0.3}$	-11.9
187811	6.5 ± 0.7	4.6 ± 0.3	3.44 ± 0.06	0.7 ± 0.1	–	–	–	–	–	–	5^{+1}_{-1}	$-12.1^{+0.2}_{-0.2}$	-11.4
189687	7 ± 2	7.1 ± 0.9	3.8 ± 0.1	0.8 ± 0.1	–	–	–	$2.2^{+0.2}_{-0.2}$	$-12.1^{+0.1}_{-0.1}$	-10.8	–	–	–
191610	5 ± 1	3.7 ± 0.6	3.3 ± 0.2	0.8 ± 0.1	4^{+4}_{-1}	-10^{+3}_{-1}	-9.1	10^{+26}_{-6}	-9^{+9}_{-2}	-8.0	$3.2^{+0.2}_{-0.2}$	$-11.2^{+0.3}_{-0.3}$	-10.7
192044	4.2 ± 0.5	5.2 ± 0.3	3.0 ± 0.1	0.76 ± 0.05	–	–	–	$3.1^{+2.3}_{-0.7}$	$-12.1^{+0.6}_{-0.3}$	-11.2	$2.2^{+0.2}_{-0.1}$	$-12.4^{+0.1}_{-0.1}$	-11.4
193911	7 ± 1	11 ± 1	3.5 ± 0.1	0.7 ± 0.1	13^{+53}_{-9}	-12^{+7}_{-1}	-10.4	–	–	–	–	–	–
194335	11 ± 2	4.4 ± 0.5	3.8 ± 0.1	0.7 ± 0.1	–	–	–	4^{+6}_{-2}	$-10.7^{+2.3}_{-0.7}$	-10.3	$3.3^{+0.2}_{-0.1}$	$-11.0^{+0.2}_{-0.2}$	-10.6
200120	12 ± 2	5.8 ± 0.7	4.1 ± 0.1	0.7 ± 0.1	–	–	–	$4.9^{+0.8}_{-0.6}$	$-9.0^{+0.7}_{-0.5}$	-8.2	$4.4^{+0.2}_{-0.2}$	$-9.5^{+0.4}_{-0.4}$	-8.7
203467	8 ± 2	9 ± 1	3.8 ± 0.1	0.7 ± 0.2	–	–	–	$1.8^{+0.1}_{-0.1}$	$-12.0^{+0.1}_{-0.1}$	-10.4	$1.70^{+0.04}_{-0.03}$	$-12.09^{+0.05}_{-0.04}$	-10.7
208682	11 ± 3	5.1 ± 1.0	3.9 ± 0.2	0.7 ± 0.1	$2.8^{+6.5}_{-0.8}$	$-11.5^{+2.4}_{-0.5}$	-10.8	–	–	–	–	–	–
209014	7 ± 2	6 ± 1	3.2 ± 0.2	0.9 ± 0.1	–	–	–	6^{+2}_{-2}	$-11.2^{+0.9}_{-0.8}$	-10.1	$2.5^{+0.2}_{-0.3}$	$-12.0^{+0.3}_{-0.3}$	-11.0
212076	10 ± 2	6.4 ± 0.7	3.7 ± 0.1	0.7 ± 0.2	–	–	–	$3.1^{+0.1}_{-0.1}$	$-10.8^{+0.2}_{-0.2}$	-9.9	$2.13^{+0.04}_{-0.03}$	$-11.7^{+0.1}_{-0.1}$	-10.8
212571	14 ± 2	6.2 ± 0.5	4.3 ± 0.1	0.7 ± 0.2	–	–	–	–	–	–	$3.5^{+0.4}_{-0.7}$	$-12.1^{+0.2}_{-0.2}$	-11.1
214748	3.4 ± 0.8	4.4 ± 0.8	2.7 ± 0.1	0.7 ± 0.1	8^{+36}_{-5}	-10^{+13}_{-2}	-9.0	$3.1^{+0.3}_{-0.3}$	$-11.7^{+0.3}_{-0.3}$	-11.0	$2.7^{+0.1}_{-0.2}$	$-11.9^{+0.2}_{-0.3}$	-11.1
217891	5.3 ± 0.9	5.5 ± 0.5	3.1 ± 0.1	0.32 ± 0.06	$2.0^{+0.2}_{-0.2}$	$-12.5^{+0.2}_{-0.2}$	-12.0	7^{+20}_{-4}	-11^{+4}_{-1}	-10.6	$2.4^{+0.1}_{-0.1}$	$-12.1^{+0.1}_{-0.2}$	-11.6
224559	7 ± 1	4.8 ± 0.6	3.3 ± 0.1	0.69 ± 0.05	–	–	–	$3.6^{+0.6}_{-0.4}$	$-10.6^{+0.5}_{-0.3}$	-9.9	$2.4^{+0.1}_{-0.1}$	$-11.5^{+0.2}_{-0.2}$	-10.8

This paper has been typeset from a \TeX/L\AA\TeX file prepared by the author.

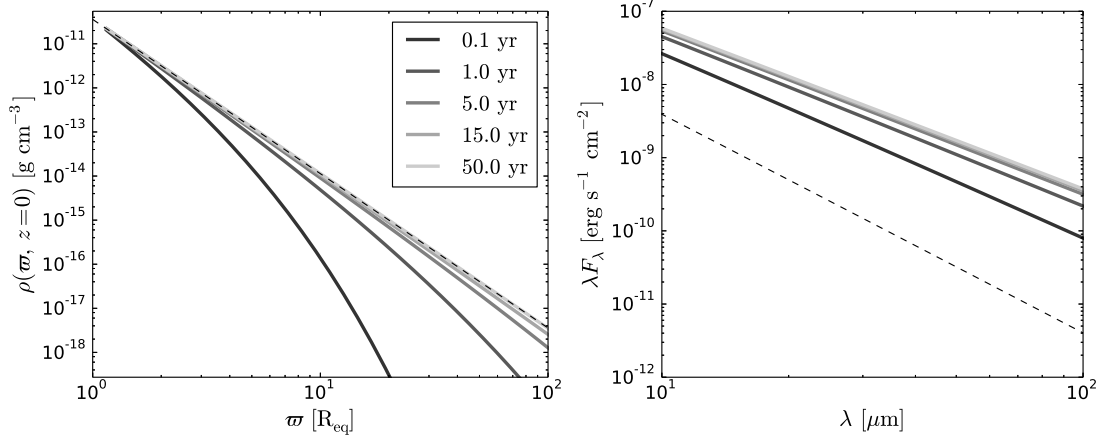
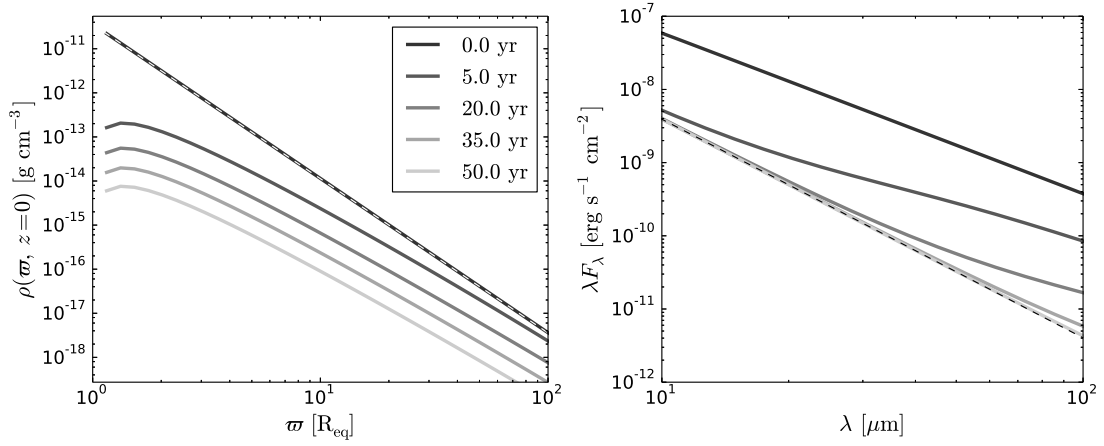
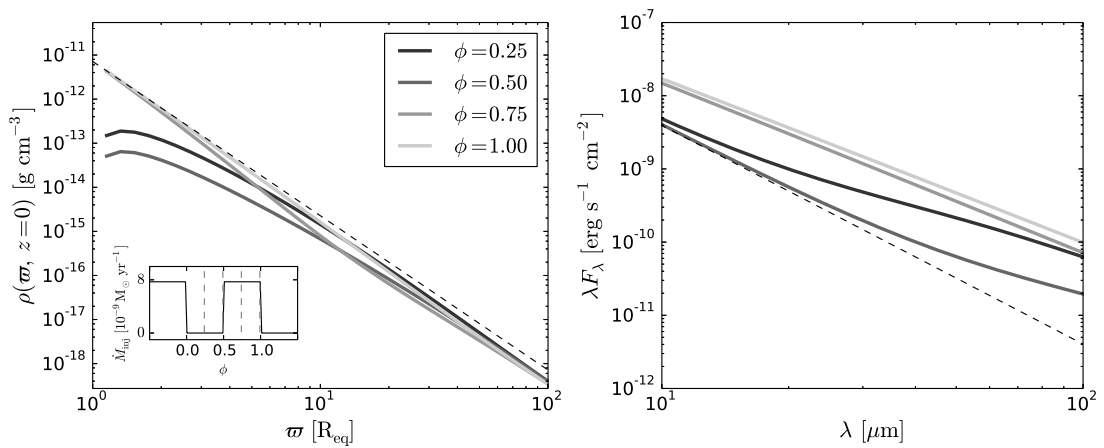

 (a) Disc build-up, with a constant mass injection rate of $3.9 \times 10^{-8} M_{\odot} \text{ yr}^{-1}$.

 (b) Disc dissipation, departing from steady-state with base density of $2.7 \times 10^{-11} \text{ g cm}^{-3}$.

 (c) Periodic mass injection with a mass injection rate of $7.7 \times 10^{-9} M_{\odot} \text{ yr}^{-1}$, a period of 5 yr and duty-cycle of 50%. The mass injection rate is shown in the subplot, where the selected phases (ϕ) are indicated. The chosen cycle corresponds to the 10th period, when the oscillatory disc properties are already stable.

Figure E2. Density profile at disc mid-plane and SED evolution for different mass injection scenarios. The dashed lines in the left panels correspond to the steady-state profile, while the dashed lines in the right panels indicate the stellar photospheric flux. For all cases, the central star has a *B2* spectral type (see Table 1), $d = 50 \text{ pc}$ and a pole-on orientation.